Revista Mexicana de Astronomía y Astrofísica, **60**, 41–67 (2024)

https://doi.org/10.22201/ia.01851101p.2024.60.01.04

THE CALAR ALTO LEGACY INTEGRAL FIELD AREA SURVEY: SPATIAL RESOLVED PROPERTIES

S. F. Sánchez[1], J. K. Barrera-Ballesteros[1], L. Galbany[2,3], R. García-Benito[4], E. Lacerda[1], and A. Camps-Fariña[5]

Received April 12 2023; accepted September 22 2023

ABSTRACT

We present the analysis using the pyPipe3D pipeline for the 895 galaxies that comprise the eCALIFA data release (Sanchez et al. 2023), data with a significantly improved spatial resolution (1.0-1.5″/FWHM). We include a description of (i) the analysis performed by the pipeline, (ii) the adopted data model for the derived spatially resolved properties and (iii) the catalog of integrated, characteristics and slope of the radial gradients for a set of observational and physical parameters derived for each galaxy. We illustrate the results of the analysis (i) using the NGC 2906 galaxy, showing the spatial distribution of the different derived parameters, and (ii) showing the distribution of the spatial resolved ionized gas across the [O_{III}]/Hβ vs. [N_{II}]/Hα diagram for the whole galaxy sample. A general agreement is found with published results, with a clear improvement in the tracing of radial patterns and the segregation of individual ionized structures. Access to all the discussed data products: http://ifs.astroscu.unam.mx/CALIFA_WEB/public_html/.

RESUMEN

Presentamos el análisis utilizando pyPipe3D en las 985 galaxies de la dstribución de datos eCALIFA (Sanchez et al. 2023), los cuales presentan una mejora significativa en la resolución espacial (1.0-1.5″/FWHM); incluimos una descripción de (i) el análisis realizado por el dataducto, (ii) el modelo de datos adoptado para las propiedades espacialmente resueltas obtenidas, y (iii) el catálogo de propiedades físicas y observacionales, integradas, caracterísiticas y las pendientes de sus gradientes radiales. Ilustramos los resultados del análisis (i) con la galaxia NGC 2906, mostramos la distribución espacial de los diferentes parámetros obtenida, y (ii) exploramos la distribución del gas ionizado espacialmente resuelto a lo largo del diagrama [O_{III}]/Hβ vs. [N_{II}]/Hα para la muestra completa de galaxias. Se reporta un acuerdo general con resultados anteriores, mejorando la determinación de patrones radiales y la segregación de estructuras ionizadas. Acceso a los productos del analisis: http://ifs.astroscu.unam.mx/CALIFA_WEB/public_html/.

Key Words: galaxies: evolution — galaxies: star formation — galaxies: stellar content — galaxies: ISM — techniques: imaging spectroscopy

1. INTRODUCTION

The Calar Alto Legacy Integral Field Area (CALIFA) project is an integral field spectroscopic (IFS) galaxy survey focused on the exploration of the spatial resolved spectroscopic properties of a statistical well defined and significant sample of galaxies in the nearby survey (Sánchez et al. 2012). It selected galaxies using their optical extension (diameter) as the primary criterion (D_{iso} ≈60″), in order to fit them within the field-of-view of the adopted integral-field unit (PPAK; Kelz et al. 2006). Besides that, the sample was restricted to a redshift range around z≈0.015, and a lower-limit to the apparent magnitude was imposed to limit the contribution of dwarf galaxies that would in other case dominate the statistics (Walcher et al. 2014). This survey gathered data for a time period between 2010 and 2016, and presented its last formal data release in Sánchez et al. (2016a). Afterwards, a set of programs continue using similar selection criteria and the same instrumental and observational setup to explore galaxies under-represented in the original sample, like companion galaxies in interacting

[1]Instituto de Astronomía, Universidad Nacional Autónoma de México, México.
[2]Institute of Space Sciences (ICE, CSIC), Campus UAB, Spain.
[3]Institut d'Estudis Espacials de Catalunya (IEEC), Spain.
[4]Instituto de Astrofísica de Andalucía (IAA/CSIC), Spain.
[5]Universidad Complutense de Madrid (UCM), Spain.

systems, cluster members, and in particular supernovae hosts (e.g. Galbany et al. 2018). All those additional subsamples of galaxies can be considered as extensions of the original sample, comprising the so-called extended CALIFA compilation (e.g. Sánchez et al. 2016a; Lacerda et al. 2020; Espinosa-Ponce et al. 2020).

In a recent companion article Sanchez et al. (2023) presented the final compilation of the extended CALIFA data set (eCALIFA), releasing the data cubes using an improved version of the data-reduction that significantly improves the spatial resolution and image quality. This data release (DR) comprises the data cubes corresponding to the V500 setup (e.g., low-resolution Sánchez et al. 2012) of 895 individual galaxies, together with a set of integrated and central aperture observational and physical parameters included in a single table [6].

Following an approach similar to that adopted in previous DRs of IFS galaxy surveys (e.g. Sánchez et al. 2022), we distribute in this paper the data products of the analysis for this data set using the `pyPipe3D` pipeline (Lacerda et al. 2022). `pyPipe3D` is a recently updated version of `Pipe3D` fully coded in `python`. The `Pipe3D` pipeline makes use of the routines and algorithms included in the `FIT3D` package (Sánchez et al. 2016c), whose main goal is to extract the properties of the ionized gas and the stellar component from IFS data in the optical range. `Pipe3D` has been frequently used to explore the data from different surveys: e.g., CALIFA (Sánchez-Menguiano et al. 2016; Espinosa-Ponce et al. 2020), SAMI (Sánchez et al. 2019b), AMUSING++ (Sánchez-Menguiano et al. 2018; López-Cobá et al. 2020) and MaNGA (Sánchez et al. 2018, 2022).

The structure of this article is as follows: (i) §2 includes a description of the explored data, with a brief summary of the data reduction; (ii) the analysis performed on the data is included in §3, comprising (iii) a summary of the main properties of `pyPipe3D` (§3.1), that includes (iii.1) a description of the adopted spatial binning (§3.1.1), (iii.2) details on the stellar population fitting (§3.1.2, (iii.3) how the emission line properties are derived (§3.1.3, (iii.4) a description of the derivation of stellar indices (§3.1.4), and finally (iii.5) how the errors of the different parameters are derived (§3.1.5) and (iii.6) the final masks generated to exclude field stars and low signal-to-noise (S/N) regions (§3.2); (iv) a description of the physical quantities derived from `pyPipe3D` data products (such as the stellar mass, $M_\star$ and the star-formation rate, SFR) is included in §3.3, with a particular description of the derivation of some kinematics parameters, such as the specific angular momentum (λ_R) included in §3.3.1; (v) Finally, we describe how we derive the integrated, characteristics and slope of radial gradients of different properties in §3.4; (vi) The results of all these analyses is included in §4, comprising a description of the adopted data format (§4.1), and each of its extensions (§4.1.1 to §4.1.6); (vii) §4.3 illustrates the content of the derived data products using NGC 2906 as an archetype galaxy, with (vii.1) a detailed exploration of the properties of the ionized gas (§4.3.1) and (vii.2) a comparison of the detectability of H II regions among the current data, the former reduced data set, and data of a much better spatial resolution (§4.3.2; (viii) an exploration of the different ionizing sources across the extension of galaxies is included in §4.4; (ix) the conclusions of the current study are included in §5.

When required along the current study, we adopted an standard Λ Cold Dark Matter cosmology with the parameters: H_0=71 km/s/Mpc, Ω_M=0.27, Ω_Λ=0.73.

2. DATA

As described previously the data analyzed in this article comprise the IFS data cubes included in the eCALIFA data release (Sanchez et al. 2023). These data were acquired using the 3.5m telescope at the Calar Alto observatory using the PPAK integral field unit (Kelz et al. 2006) of the PMAS spectrograph (Roth et al. 2005). All observations were performed with the V500 grating, set up at the same goniometer angle, using a similar exposure time and the same dithering scheme (to cover completely the FoV) as the one designed and adopted by the CALIFA survey (Sánchez et al. 2012, 2016a, for more details). This setup allows to cover a wavelength range between 3745-7500Å, with a spectral resolution of R≈850 (FWHM ≈6.5Å), covering an hexagonal area of $74'' \times 64''$.

The data were reduced using version 2.3 of the CALIFA pipeline, described in detail in Sanchez et al. (2023), and previous studies (Sánchez 2006; García-Benito et al. 2015; Sánchez et al. 2016a). We present here a brief summary of the most relevant steps: (i) pre-processing the raw data to join in a single frame the data read by different amplifiers, removing the bias, normalizing by the GAIN, and cleaning for cosmic-rays, (ii) identifying and tracing the spectra corresponding to different fibers in the CCD, obtaining the width of the light projected along the dispersion and cross-dispersion axis, (iii) extraction of the spectra using the trace and widths estimated during the previous setup, removing the effects of the stray-light, (iv) performing a wavelength calibration and re-sampling of the data to follow a linear wavelength solution (2Å/spectral pixel), (v) homogenization of the spectral resolution along the wavelength range fixing the final resolution to FWHM = 6.5Å, (vi) correcting for the differential fiber-to-fiber transmission, (vii) flux-calibrating

[6] `http://ifs.astroscu.unam.mx/CALIFA_WEB/public_html/`.

the spectra, (viii) separating the science fibers, covering the central hexagonal region, from those fibers that sample the sky (and those coupled to the calibration), generating and subtracting a night-sky spectrum for each dither pointing, (ix) glueing the three dithering pointings into a single spectral frame with its corresponding position table, (x) derivation of the astrometric solution for each dithering pointing using the data from the PanStarrs survey as astrometry reference (PS; Chambers et al. 2016; Flewelling et al. 2020), correcting the nominal position table based on this registration, (xi) correcting of the broken fibers and vignetted regions of the spectra using the information of adjacent fibers, and finally (xii) implementing a new image reconstruction procedure that modifies the previously adopted interpolation kernel (Sánchez et al. 2016a), introduces a low-order deconvolution procedure, and a final monochromatic flat-fielding.

The major differences of this new reduction procedure with respect to previous versions are introduced in the last three steps. As a result a considerable improvement in the image quality and the final spatial resolution is obtained, that approaches that provided by the natural seeing (FWHM$_{psf}$ $\approx$1.5″, on average). This improved spatial resolution requires that the new data cube have a smaller spaxel size (0.5″/spaxel) for a proper sampling of the point-spread-function (PSF). This is half of the size of the CALIFA data cubes delivered in previous DR (Husemann et al. 2013; García-Benito et al. 2015; Sánchez et al. 2016a). Finally, the absolute photometry is anchored to that of the PS survey, in contrast to previous reductions in which the Sloan Digital Sky Survey (SDSS York et al. 2000) photometry was adopted.

The final data set, once a set of quality control criteria is established, comprises 895 cubes, each one corresponding to an individual galaxy. Sanchez et al. (2023) demonstrate that this compilation, covering a wide range of galaxy morphologies and masses ($\approx 10^7$-10^{12} M$_\odot$), behaves as a diameter selected sample, being roughly representative of the population of galaxies in the nearby universe ($z \approx 0.015$). For more details on the data reduction, its quality and the properties of the sample we refer the reader to Sanchez et al. (2023).

3. ANALYSIS

As indicated before, the analysis performed on the described dataset follows Sánchez et al. (2022). We estimate the main spatial resolved, characteristics and integrated properties of each galaxy by applying `pyPipe3D` to each data cube. Then, the data products provided by this pipeline were processed to obtain a set of physical quantities. We integrated them galaxy-wide, and explored their radial distributions to derive their value at the effective radius (*Re*), i.e., the characteristic value, and the radial gradient. We present here a brief summary of the analysis and the derived quantities, referring to previous publications for more details to avoid repetition (in particular to Sánchez et al. 2016a, 2021, 2022).

3.1. `pyPipe3D` *Analysis*

We use `pyPipe3D` (Lacerda et al. 2022), the new version of the `Pipe3D` pipeline (Sánchez et al. 2016b). This version adapts to python the algorithms and analysis sequence of the precedent one, improving its performance thanks to the computational capabilities of this coding language, and correcting some bugs when necessary. `Pipe3D` is a well-proved pipeline, that has been used to study IFS data from different data sets, including the massive exploration of CALIFA (e.g. Cano-Díaz et al. 2016; Espinosa-Ponce et al. 2020), MaNGA (e.g. Ibarra-Medel et al. 2016; Barrera-Ballesteros et al. 2018; Sánchez et al. 2019a; Bluck et al. 2019; Sánchez-Menguiano et al. 2019), SAMI (e.g. Sánchez et al. 2019b), and AMUSING++ data sets (Sánchez-Menguiano et al. 2018; López-Cobá et al. 2020). Besides that, it has been tested using mock data sets and ad-hoc simulations based on hydrodynamical simulations (Guidi et al. 2018; Ibarra-Medel et al. 2019; Sarmiento et al. 2022). We present here just a brief description of the code to avoid unnecessary repetitions.

3.1.1. *Spatial Binning/Tessellation*

`pyPipe3D` pipeline uses the algorithms included in the `pyFIT3D` package to analyze automatically each data cube. However, to provide a reliable result in the analysis of the stellar population (that we will describe below) it is required to perform a spatial binning to increase the signal-to-noise (S/N) above a minimum value (see Sánchez et al. 2016c; Lacerda et al. 2022, for details). The binning procedure adopted by `pyPipe3D` preserves the shape of the original light distribution to a larger extent than other methods frequently implemented in the literature (see Sánchez et al. 2016c, for detailed discussion on the topic). Then the fitting procedure is applied to each binned spectrum, recovering the parameters of the stellar population and emission lines in each tessella/spatial-bin.

We need to recall that the new reduced data (Sanchez et al. 2023), have a spaxel scale 4-times smaller than the original ones. Besides, the whole image reconstruction algorithm has changed considerably. This means that the covariance pattern between adjacent spaxels has changed too. Thus, a new covariance correction has to be introduced during the binning/tessallation process, as discussed in §5.4 of Sanchez et al. (2023), shown in Figure 26. The code has been modified to take into account this modification.

3.1.2. *Stellar Population Analysis*

As already mentioned, each binned spectrum is analyzed using pyFIT3D. This code separates the stellar and ionized-gas emission in each spectrum by creating a model of the former one using a linear combination of a set of pre-defined single stellar populations (SSP) spectra (S_{ssp}). Following Sánchez et al. (2022) and Sanchez et al. (2023), we use the MaStar_sLOG SSP library for the current analysis. This library comprises 273 SSP templates with 39 ages, $\mathcal{A}_\star$/Gyr = (0.001, 0.0023, 0.0038, 0.0057, 0.008, 0.0115, 0.015, 0.02, 0.026, 0.033, 0.0425, 0.0535, 0.07, 0.09, 0.11, 0.14, 0.18, 0.225, 0.275, 0.35, 0.45, 0.55, 0.65, 0.85, 1.1, 1.3, 1.6, 2, 2.5, 3, 3.75, 4.5, 5.25, 6.25, 7.5, 8.5, 10.25, 12, 13.5), and 7 metallicities, $Z_\star$ = (0.0001, 0.0005, 0.002, 0.008, 0.017, 0.03, 0.04). Details on the library and its ingredients are included in Appendix A of Sánchez et al. (2022). Before doing this modelling, the SSP templates are shifted and broadened to take into account the systemic velocity ($v_\star$) and the velocity dispersion ($\sigma_\star$), assuming that the line-of-sight velocity distribution follows a Gaussian distribution $G(v_\star, \sigma_\star)$. In addition, the dust attenuation affecting the stellar populations ($A_{V,\star}$) is modelled using the Cardelli et al. (1989) extinction law ($E(\lambda)$). The derivation of these three parameters is performed by selecting a limited sub-set of the SSP spectra that limits the range of ages and metallicities, avoiding possible degeneracies.

Then, the shifted, broadened and dust attenuated SSP templates are fitted to the data by an iterative set of linear decompositions that includes or removes templates into the library forcing the procedure to provide only positive coefficients ($w_{ssp,\star,L}$) in the linear decomposition as explained in Sánchez et al. (2016c) and Lacerda et al. (2022). Finally, the observed spectrum (S_{obs}) is fitted by a stellar model (S_{mod}) that follows the expression

$$S_{obs}(\lambda) \approx S_{mod}(\lambda) = \left[\sum_{ssp} w_{ssp,\star,L} S_{ssp}(\lambda)\right] 10^{-0.4\, A_{V,\star}\, E(\lambda)} * G(v_\star, \sigma_\star). \quad (1)$$

In the particular implementation for the current analysis the light-fractions or weights of the stellar population decomposition (i.e., $w_{\star,L}$), are normalized to the 5450-5550Å spectral range (approximately the $V-$band central wavelength).

pyFIT3D derives the luminosity- and mass-weighted parameters of the stellar population (P_{LW} and P_{MW}) with the coefficients of the stellar decomposition described before, using the equation:

$$\log P_{LW} = \sum_{ssp} w_{ssp,\star,L} \log P_{ssp} \,,$$
$$\log P_{MW} = \frac{\sum_{ssp} w_{ssp,\star,L} \Upsilon_{ssp,\star} \log P_{ssp}}{\sum_{ssp} w_{ssp,\star,L} \Upsilon_{ssp,\star}} \,, \quad (2)$$

where P_{ssp} is the value of a particular parameter for each SSP (for instance, age, $\mathcal{A}_\star$, or metallicity, $\mathcal{Z}_\star$), and $\Upsilon_{ssp,\star}$ is the stellar mass-to-light ratio. It also estimates the stellar mass across the considered aperture, using the equation:

$$M_\star = L_V \sum_{ssp} w_{ssp,\star,L} \Upsilon_{ssp,\star} \,, \quad (3)$$

where L_V is the dust-corrected V-band luminosity.

3.1.3. *Emission Line Analysis*

To derive the properties of the ionized gas emission the code subtracts the best stellar population model from the observed one. Then, it fits each emission line (*el*) extracted from a pre-defined list [7] with a Gaussian function ($G(vel_{el}, \sigma_{el})$, where v_{el} and σ_{el} are the *el* velocity and velocity dispersion, respectively, scaled by the integrated flux intensity (F_{el}). The bulk procedure (analysis of stellar population and emission lines) is repeated iteratively, using the best emission line model to decontaminate the original spectrum that then is modelled by the combination of SSPs. In each iteration the χ^2, considering both the stellar population and emission line model, is adopted as the figure of merit of the quality of the fitting.

The described procedure provides the properties of the emission lines for each tessella/spatial-bin. In order to recover the properties of the emission lines spaxel-wise, an additional procedure is implemented. First, the best fitted stellar population model derived for each tessella is scaled to each spaxel within the bin using the so-called dezonification parameter (DZ, Cid Fernandes et al. 2013). Then this spaxel-wise stellar population model is subtracted from the original data cube to create the so-called pure-GAS cube, which comprises the emission from the ionized gas, plus noise and residuals of the stellar population fitting. Finally, two different procedures are implemented to extract the parameters of the ionized gas emission lines from this cube: (i) a Gaussian model similar to the one described before is applied to the strongest emission lines in the wavelength range (listed before); and (ii) a weighted-moment analysis is performed for a large set of emission lines, including both the strong and weak emission lines. Both methods provide the same three parameters (F_{el}, v_{el} and σ_{el}). However, the second one determines also the equivalent width of each analyzed emission line (EW_{el}). The complete list of emission lines analyzed using this latter method will be described later (§ 4.1.5).

3.1.4. *Stellar Indices*

In addition, pyPipe3D estimates a set of the stellar indices for each voxel/tessella. For doing so, a stellar

[7] In this analysis, [O II]λ3727, Hδ, Hγ, Hβ, [O III]$\lambda\lambda$4959,5007, Hα, [N II]$\lambda\lambda$6548,84 and [S II]$\lambda\lambda$6717,31

spectrum is first generated, decontaminated by the ionized gas contribution by removing the best emission line model derived along the fitting procedure described before. Afterwards, the equivalent width is derived for each stellar index defining three wavelength ranges: (i) a central one at which the stellar index is defined, and (ii) two adjacent ones at which the density flux of the continuum is estimated. The particular list of stellar indices included in the current analysis is described in §4.1.3.

3.1.5. *Error Estimation*

The errors of all the derived parameters are estimated by performing a Monte Carlo (MC) procedure. Each original spectrum (spaxel-wise or binned) is perturbed by co-adding a random value using the errors provided by the data reduction. Then, the full procedure is repeated for each perturbed spectrum, defining the errors as the standard deviation of the individual values derived for each set of modified spectra. We should note that when an ionized-gas or stellar population model is subtracted from the original spectrum the errors are updated, considering the uncertainties of the model. For more details on the estimation of the errors we refer the reader to Lacerda et al. (2022).

Once more we remind the reader that the new data reduction introduces a new image reconstruction scheme that improves the spatial resolution, and therefore the data cubes have a spaxel size two times smaller than the one adopted in previous reductions: 0.5″/spaxel Sanchez et al. (2023), rather than 1.0″/spaxel (Sánchez et al. 2016a). Thus, the flux per spaxel at any wavelength is now four times smaller than in the previous versions of the data reduction. On the other hand, the S/N per arcsec^2 is roughly the same in the two versions of the data reduction, as seen when comparing Figure 5 of Sanchez et al. (2023) with Figure 14 of Sánchez et al. (2016a). Therefore, the S/N per spaxel is ≈4 times lower at any wavelength in the new data set, what affects equally the continuum and emission lines. This has to be taken into account in any spatial resolved analysis performed with the new data products.

3.2. *Data Masks*

The errors of each parameter, and in particular the error of the flux intensity, are used to define different masks. In the case of the continuum, we select those regions above a signal-to-noise ratio of one prior to the spatial binning described in §3.1.1. This defines a selection mask that is applied prior to any analysis of the stellar population properties. In addition to this mask, regions strongly affected by foreground field stars should be masked too. As we describe in Sanchez et al. (2023) we follow the procedure included in Sánchez et al. (2022), searching for possible foreground field stars in the FoV of the analyzed datacubes, using the Gaia DR3 catalog[8] (Gaia Collaboration et al. 2016, 2021). This catalog comprises the most accurate and complete list of stars with good quality astrometry covering the full sky. Only those sources with an accurate parallax (five times larger than the uncertainty) are selected, and we generate a circular mask of 2.5″ around each of them. This mask is then used ignoring the values reported by the analysis in those regions and replacing them by an interpolated version of the values in the adjacent spaxels.

3.3. *Physical Quantities*

The observational properties estimated by `pyPipe3D` for each spaxel or tessella within the data cubes for both the stellar populations an ionized gas emission lines are used to estimate further physical parameters. Details of the derivation of all them have been extensively discussed in previous articles, in particular in Sánchez et al. (2021) and Sánchez et al. (2022). We provide here with a brief summary to avoid repetition:

Stellar Masses: The stellar mass is derived directly by `pyFIT3D` as one of the quantities directly estimated from the stellar decomposition analysis, as indicated in §3.1.2. From this estimation is derived the stellar mass density ($\Sigma_\star$), and the corresponding values in different apertures. Based on this value it is possible to derive the integrated $\Upsilon_\star$ (i.e., $M_\star/L_\star$ for each spaxel), that is different than the LW or MW average value that would be provided by equation 2.

Star-formation and chemical enrichment histories: Equations 2 and 3 can be integrated up to a certain look-back time, correcting for the mass loss when needed (e.g. Courteau et al. 1996), obtaining the mass-assembly (MAH, Pérez et al. 2013; Ibarra-Medel et al. 2016, 2019), star-formation (SFH, Panter et al. 2007; González Delgado et al. 2017; López Fernández et al. 2018; Sánchez et al. 2019a), and chemical-enrichment histories (ChEH, Vale Asari et al. 2009; Camps-Fariña et al. 2021, 2022). From those distributions we estimate (i) the current SFR ($SFR_{ssp,t}$), by restricting the SFH to the most recent (short) time scales (e.g., $SFR_{ssp,10Myr}$, average SFR in the last 10 Myr), (ii) a set of time-scales that characterize the SFHs, defined as the time in which a fraction of the stellar mass is formed (`T%`, e.g., T80, time in which 80% of the stellar mass was formed); and (iii) the metallicity at those time scales (`a_ZH_T%`).

Emission line ratios: line ratios are frequently used to estimate the nature of the ionizing source and the physical properties of the ionized gas itself. From the emission line fluxes derived using the moment analysis we estimate a set of line ratios including the most popular

[8] https://www.cosmos.esa.int/web/gaia/dr3

ones, namely [O II]/Hβ, [O III]/Hβ, [O I]/Hα, [N II]/Hα, [S II]/Hα and Hα/Hβ.

Ionized gas dust extinction: The Hα/Hβ line ratio is used to estimate the dust extinction ($A_{V,gas}$). To do so we adopt a nominal ratio for Hα/Hβ of 2.86, that corresponds to case-B recombination with an electron density of n_e=100 cm^{-3} and a temperature of T_e=10^4 K (Osterbrock 1989). The Cardelli et al. (1989) dust attenuation law was applied, with a total-to-selective extinction value of R_V =3.1.

Oxygen and nitrogen abundances and ionization parameter: the line ratios described before are frequently used to estimate the oxygen and nitrogen abundances and the ionization parameter using strong-line calibrators. These calibrators are only valid for those ionization sources for which they are derived (i.e., regions ionized by OB stars related with recent SF events). We classify the ionizing source following Sánchez et al. (2021), selecting as SF regions those located below the demarcation line defined by Kewley et al. (2001) in the [O III]/Hβ vs [N II]/Hα diagnostic diagram with an EW(Hα)> 3Å. Then, for those regions we estimate the oxygen (O/H) and nitrogen (N/H and/or N/O) abundance and the ionization parameter (U) using a set of strong-line calibrators. In total we use 28 calibrators for the oxygen abundances, 3 calibrators for the nitrogen abundance and 4 for the ionization parameter. The complete list of calibrators, the line ratios that are used to derive them, and a detailed description of their nature is included in Sánchez et al. (2022, in particular in Appendix D and Table 15). We refer the reader to that reference to avoid repetition.

Hα based star-formation rate: The SFR is derived spaxel-wise using the Kennicutt (1998) relation between this quantity and the dust-corrected Hα luminosity:

$$\mathrm{SFR}\ (M_\odot\ yr^{-1}) \ = \ 0.79\ 10^{-41}\ \mathrm{L_{H\alpha}}\ (erg/s). \qquad (4)$$

This relation corresponds to a Salpeter (1955) IMF. Like in the case of other extensive quantities (e.g. $M_\star$), from the SFR estimated at each spaxel it is possible to derive the SFR surface density (Σ_{SFR}), and the corresponding quantities at different apertures. Following Sánchez et al. (2021) we derive the SFR for all spaxels, irrespective of its ionizing source. However, it is possible to select only those regions compatible with being ionized by young massive OB-stars (as indicated in the previous section) in the derivation of the integrated or aperture limited SFR. A correction to the possible contribution of other ionizing sources can also be applied, either applying a mask that exclude the contaminating regions or estimating its contribution. Following Sánchez et al. (2022) we also estimate the SFR decontaminated from the contribution of the diffuse ionization due to old/evolved post-AGB stars (e.g. Singh et al. 2013).

Molecular gas estimation: we use the recent calibrators proposed by Barrera-Ballesteros et al. (2020) and Barrera-Ballesteros et al. (2021) to estimate the molecular gas mass density from the dust attenuation:

$$\begin{aligned} \Sigma_{\mathrm{mol}}\ (M_\odot\ pc^{-2}) \ &= \ 23\ A_{\mathrm{V,gas}}\ (mag)\ , \\ \Sigma_{\mathrm{mol}}\ (M_\odot\ pc^{-2}) \ &= \ 1.06\ A_{\mathrm{V,gas}}^{2.58}\ (mag)\ . \end{aligned} \qquad (5)$$

Different variations of this calibrator have been applied, including possible corrections taking into account the EW(Hα), the oxygen abundance, and using as tracer of the gas the dust attenuation derived for the stellar populations ($A_{V,\star}$) and the ionized gas ($A_{V,gas}$).

Electron density: The electron density is derived spaxel-wise using the [SII]λ6717,31 line ratio solving the equation:

$$\frac{\mathrm{[SII]}\lambda6717}{\mathrm{[SII]}\lambda6731} = 1.49\frac{1+3.77x}{1+12.8x}, \qquad (6)$$

where $x = 10^{-4} n_e t^{-1/2}$, with t being the electron temperature in units of 10^4 K (McCall et al. 1985), and n_e being the electron density in units of cm^{-3}. We solve this equation assuming a temperature of $T_e = 10^4$ K (i.e., t =1). As the dependence of the electron density with T_e is rather weak this assumption does not affect significantly the derivation of this parameter.

3.3.1. *Kinematics Parameters*

`pyPipe3D` provides the spatial distribution of the stellar and gas velocity and velocity dispersion. From these distributions we estimate (i) the velocity to velocity dispersion ratio $\left(\frac{v}{\sigma}_R\right)$ for both the stellar and ionized gas components, and (ii) the apparent stellar angular momentum parameter (λ_R) at different deprojected galactocentric distances (R). For $\frac{v}{\sigma}_R$ we adopt the formula:

$$\frac{v}{\sigma} = \sqrt{\frac{\sum_{r<1Re} f_\star v_\star^2}{\sum_{r<1Re} f_\star \sigma_\star^2}}, \qquad (7)$$

where $f_\star$ is the stellar flux intensity in the V-band, and $v_\star$ and $\sigma_\star$ are the the velocity and velocity dispersions. A similar formula is adopted for the ionized gas, changing each parameter in eq. 7 by the corresponding values derived for the Hα emission lines. Finally, for λ_R we followed Emsellem et al. (2007), using the formula:

$$\lambda_{\mathrm{R}} = \frac{\sum_{R<1.15Re} f_\star\ r\ |v_\star|}{\sum_{r<1.15Re} f_\star\ R\ \sqrt{v_\star^2+\sigma_\star^2}}, \qquad (8)$$

where $f_\star$, $v_\star$ and $\sigma_\star$ are the same parameters adopted in Eq. 7. An inclination correction was applied, following

the prescriptions included in the Appendix of Emsellem et al. (2011).

We should note that the spectral resolution of the current data, that corresponds to σ_{inst} ≈150 km s^{-1}, is not optimal to derive these kinematics paramters, in particular in the regime of low velocity dispersion.

3.4. *Integrated, Aperture Limited and Characteristic Properties*

The analysis described so far provides a set of parameters for each individual spaxel, tessella, or as a function of the galactocentric distance. Based on those distributions we estimate for the extensive quantities (e.g., $M_\star$ or SFR) the values at different apertures: integrated galaxy wide, the value within 1 *Re*, or in the central aperture (1.5″/diameter). For the intensive quantities (e..g, $\Sigma_\star$, the oxygen abundance or any of the analyzed stellar indices), we estimate the azimuthal average radial distribution as described in Sánchez et al. (2021) and Barrera-Ballesteros et al. (2022). Essentially, we use the coordinates of the galaxy, the position angle and ellipticity to trace a set of elliptical apertures of 0.15 *Re* width, from 0 to 3.5 *Re* (or the edge of the FoV). Then, for each aperture we estimate the average value of the corresponding parameter (P_R) and its standard deviation (e_P_R). Then, for each of those radial distributions we perform a linear regression to estimate the value at the effective radius (P_{Re}) and the slope of the gradient (*slope_P*). As already discussed in previous studies, for many parameters the value at the effective radius can be considered a good characterization of the average value galaxy-wide (e.g. Sánchez et al. 2021, and references therein). For completeness, for some intensive parameters we derive the value in the central aperture and the average value galaxy-wide.

4. RESULTS

Along this section we describe the results from the analysis outlined in the previous section, including a description of the delivered data products, together with some examples that illustrate their possible scientific use, highlighting the improvements introduced by the new distributed data set.

4.1. *Pipe3D Data Model*

The analysis described in §3.1 provides a list of parameters estimated at each individual spaxel or within a tessella with their corresponding errors. Thus, for each data cube the analysis provides a set of maps or 2D arrays for each parameter, whose astrometry and dimensions correspond to that of the analyzed data cube. Following Sánchez et al. (2016b, 2018, 2022) we group those maps depending on the analysis that produced them and pack them in a set of 3D arrays or cubes of data products. This way, each channel in the z-axis of each cube corresponds to the spatial distribution of one particular parameter. Finally, each of those `pyPipe3D` data cubes is stored as an extension of the same FITS file for its distribution.

For the data analyzed along this study the Pipe3D files comprise nine extensions for each derived FITS file: (i) ORG_HDR, an initial extension without data, containing all the metadata of the analyzed datacube, in particular the astrometric solution (world coordinate system); (ii) SSP, comprises the spatial distributions of the average stellar properties derived by the stellar population fitting (§3.1.2); (iii) SFH, includes the spatial distribution of the coefficients $w_{\star,L}$ of the fitting of the stellar population with the templates adopted SSP library (i.e., Eq. 1); (iv) INDICES, includes the spatial distribution of the stellar indices (§3.1.4); (v) ELINES, comprises the properties of the strong emission lines derived by fitting them with a set of Gaussian functions (§3.1.3); (vi) FLUX_ELINES and (vii) FLUX_ELINES_LONG include the parameters of the emission lines derived using a weighted-moment analysis (§3.1.3), for a two subsets of emission lines. In the first case we use the list of 54 emission lines adopted in a previous analysis of the CALIFA data using Pipe3D (Sánchez et al. 2016b). In the second case we adopt a larger list of emission lines, with an updated value for the rest-frame wavelength, included in Sánchez et al. (2022), adapted for the more limited wavelength range of the current data (with a total of 130 emission lines); (viii) GAIA_MASK, mask of the field stars derived from the Gaia catalog described in §3.2, and finally (ix) SELECT_REG, mask of the regions with signal-to-noise larger than 3 in the stellar continuum (V-band), i.e., those regions where the analysis of the stellar population is reliable. A summary of the format of the FITS file is presented in Table 1. For each analyzed galaxy (`CUBENAME`.V500.drscube.fits.gz) we provide one of those files, adopting the nomenclature `CUBENAME`.Pipe3D.cube.fits.gz. The entire list of data products files is distributed in the eCALIFA data release webpage [9]

4.1.1. *SSP Extension*

This extension comprises the datacube in which are stored: (i) the average properties of the stellar populations derived by `pyPipe3D` based on the decomposition of the stellar population on a set of SSP templates ($\mathcal{A}_{\star,L}$, $\mathcal{A}_{\star,M}$, $\mathcal{Z}_{\star,L}$ and $\mathcal{Z}_{\star,M}$), (ii) parameters such as the stellar mass and the $\Upsilon_\star$, (iii) the non-linear parameters ($v_\star$, $\sigma_\star$ and $A_{V,\star}$), and (iv) additional parameters describing the light distribution, the binning pattern, and the dezonification scaling applied during the fitting procedure. As the

[9] `http://ifs.astroscu.unam.mx/CALIFA/V500/v2.3/pyPipe3D/`

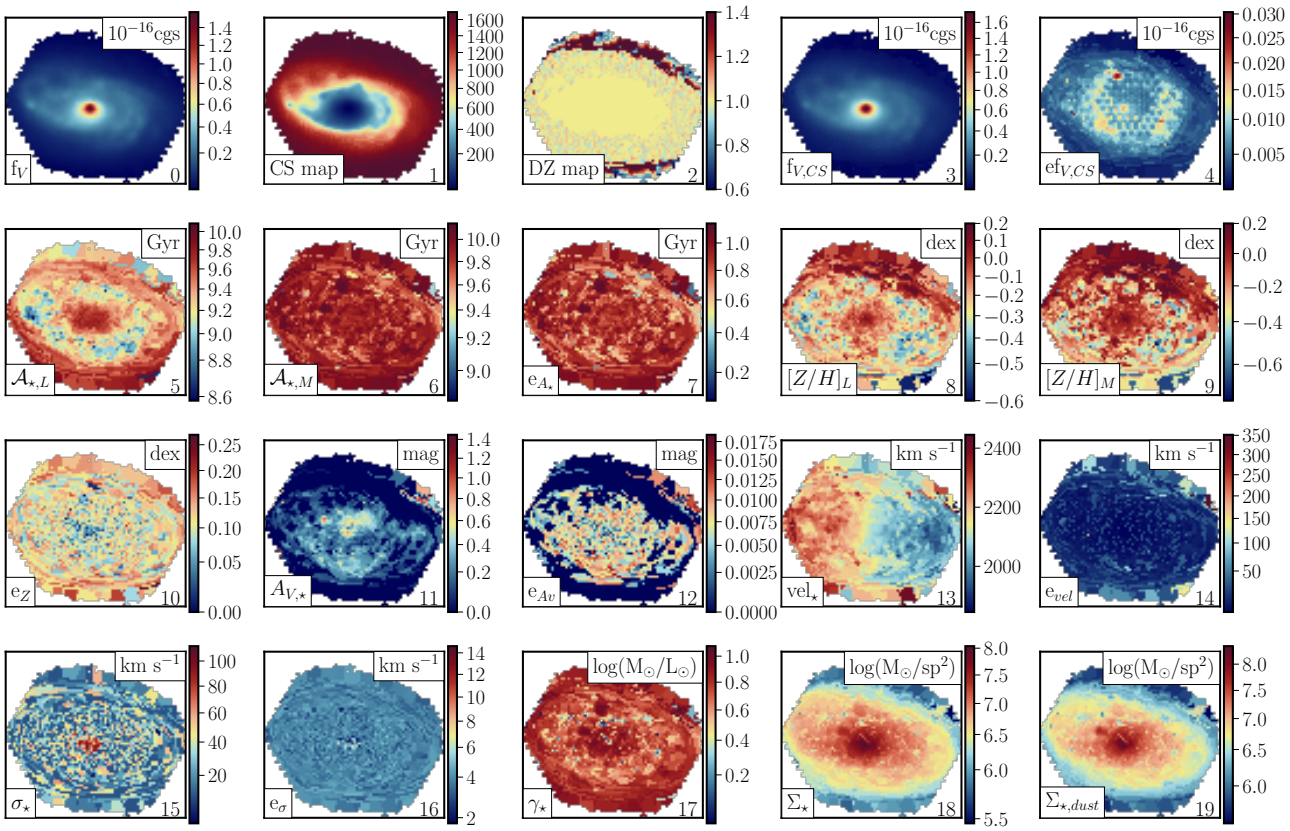

Fig. 1. Example of the content of the SSP extension in the Pipe3D fitsfile, corresponding to the galaxy NGC2906. Each panel shows a color image with the property stored in the corresponding channel of the data cube, as listed in Table 2. The index, corresponding property, and units, are indicated in each panel as a label at bottom-right, bottom-left and top-right of the figure. The color figure can be viewed online.

TABLE 1

DESCRIPTION OF THE PIPE3D FILE

HDU	EXTENSION	Dimensions
0	ORG_HDR	()
1	SSP	(NX, NY, 21)
2	SFH	(NX, NY, 319)
3	INDICES	(NX, NY, 70)
4	ELINES	(NX, NY, 11)
5	FLUX_ELINES	(NX, NY, 432)
6	FLUX_ELINES_LONG	(NX, NY, 1040)
7	GAIA_MASK	(NX, NY)
8	SELECT_REG	(NX, NY)

NX and NY may change from galaxy to galaxy, being ≈160 and ≈150 respectively.

stellar population analysis is performed on the spatial-binned data cube, the parameters stored in this extension reflect this binning. Thus, apart from the original light distribution and the dezonication scale, all parameters are equal within each considered tessella.

Table 2 describes the parameter delivered in each channel (starting with 0), and its corresponding units (when required). This information is included in a set of header keywords labelled `DESC_N`, with `N` corresponding to each channel in the z-axis. Figure 1 illustrates the content of this extension, showing for each channel the spatial distribution of the stored parameter corresponding to the galaxy NGC 2906, an archetypal spiral galaxy included in the analyzed sample. Some patterns known for this kind of galaxies, like radial gradients in the $\mathcal{A}_{\star,L}$ and $\mathcal{Z}_{\star,L}$, the drop $\sigma_\star$ from the bulge outwards, and the clear rotational pattern seen in the $v_\star$ map, are evident in this figure. Like in previous sections, for more details on each parameter we refer the reader to Sánchez et al. (2022).

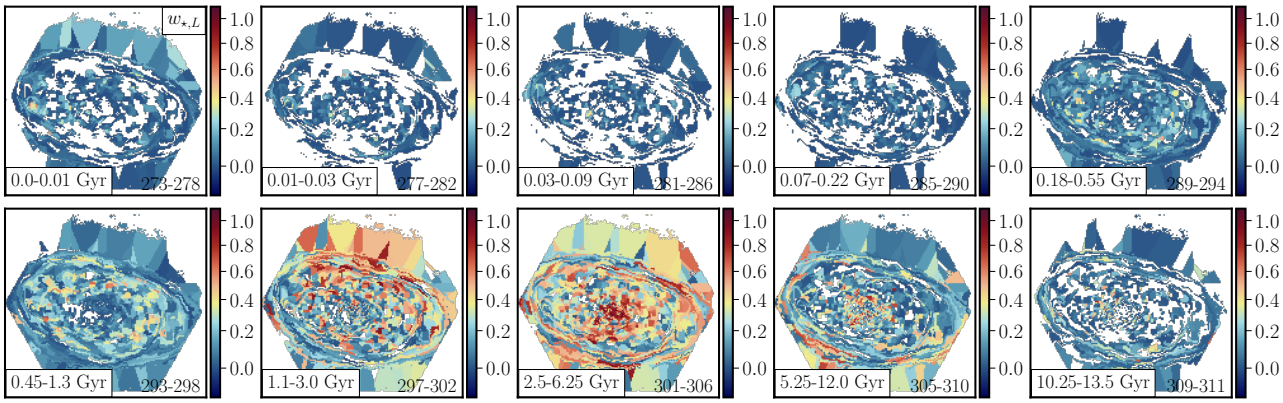

Fig. 2. Example of the content of the SFH extension in the Pipe3D fitsfile, corresponding to the galaxy NGC2906. Each panel shows a color image with the fraction of light at the normalization wavelength ($w_{\star,L}$) for different ranges of age included in the SSP library. The range of ages is indicated in the bottom-left inbox, and the corresponding indices of the co-added channels in the SFH extension are shown in the bottom-right legend. For instance, the top-left panel corresponds to the co-adding of all the maps in the SFH_CUBE from the 273 to the 278, covering the age range between zero and 0.01 Gyr. As described in §4.1.2 and shown in Table 3, these channels run for the indices from 273 to 311, and they corresponds to light-weight maps at a fixed age (each channel) derived by co-adding all the light-weighted maps for the seven different metallicities at that particular age. . For clarity we do not show the individual $w_{\star,L}$ maps included in the SFH extension , as this would require a plot with a total of 318 panels, that would not add any relevant information. The color figure can be viewed online.

4.1.2. *SFH Extension*

The data cube stored in this extension includes the spatial distribution of the coefficients of stellar decomposition for each SSP template in the adopted library, i.e., $w_{\star,L}(\mathcal{A}_\star,\mathcal{Z}_\star)$ in Eq. 1. Thus, the first 273 channels cover the total range of ages (39) and metallicities (7) included in the adopted SSP template (`MaStar_sLOG`). In addition 39 additional channels are included comprising the weights corresponding to each age, i.e., $w_{\star,L}(\mathcal{A}_\star)$, obtained by co-adding all $w_{\star,L}$ corresponding to the same age covering the seven different metallicites (channels from 273 to 311). Finally, 7 additional channels are also included with the weights corresponding to each metallicity, i.e., $w_{\star,L}(\mathcal{Z}_\star)$, obtained by co-adding all $w_{\star,L}$ corresponding to the same metallicity and covering the 39 different ages (channels from 311 to 318). Table 3 lists the content of each channel in this extension, information included in a set headers keywords named DESC_N, with N indicating the actual channel (running from 0 to 318)

Figure 2 illustrates the content of this extension, showing the spatial distribution of the weights for each age, $w_{\star,L}(\mathcal{A}_\star)$, re-binned in a set of 10 age ranges. This figure illustrates how the age distribution of the stellar population changes with the galactocentric distance, with a larger (smaller) fraction of light corresponding to older (younger) stellar populations, e.g., $\mathcal{A}_\star$ >2.5Gyr (<300 Myr) is more concentrated in the inner (outer) regions.

As described in Lacerda et al. (2022) and summarized in §3.1.5, `pyPipe3D` includes a procedure to estimate the errors of any derived quantity based on a MC procedure. However, for the current extension we decided not to distribute the errors as it would unnecessarily increase the size of this extension beyond the reasonable (due to the number of channels involved). Instead, we recommend the user to estimate the errors from the data themselves. The procedure to do so uses the covariance between adjacent spaxels, estimating the error as the standard deviation within in a box of the size of the PSF FWHM (≈1.5″ on average Sanchez et al. 2023) of the residuals once subtracted from the map corresponding to each channel a smoothed version with a Gaussian function of the size of the PSF. This calculation relies on the fact that no parameter should change significantly within the size a resolution element (i.e., the PSF), and therefore, the observed variations spaxel by spaxel should be representative of the error. On average, the typical error of $w_{\star,L}(\mathcal{A}_\star,\mathcal{Z}_\star)$ for the average S/N of our spectra is of the order of 30-50%, which corresponds to ≈20% (≈10%) error for $w_{\mathcal{A}_\star}$ ($w_{\mathcal{Z}_\star}$) [10].

4.1.3. *INDICES Extension*

As described in §3.1.4, `pyPipe3D` estimates the spatial distribution of a set of stellar indices, using the

[10]The procedure is included in the following notebook `https://github.com/sfsanchez72/califa_v2.3/blob/main/CALIFA_eDR_pyPipe3d.ipynb`, used to create figures in §4.1.

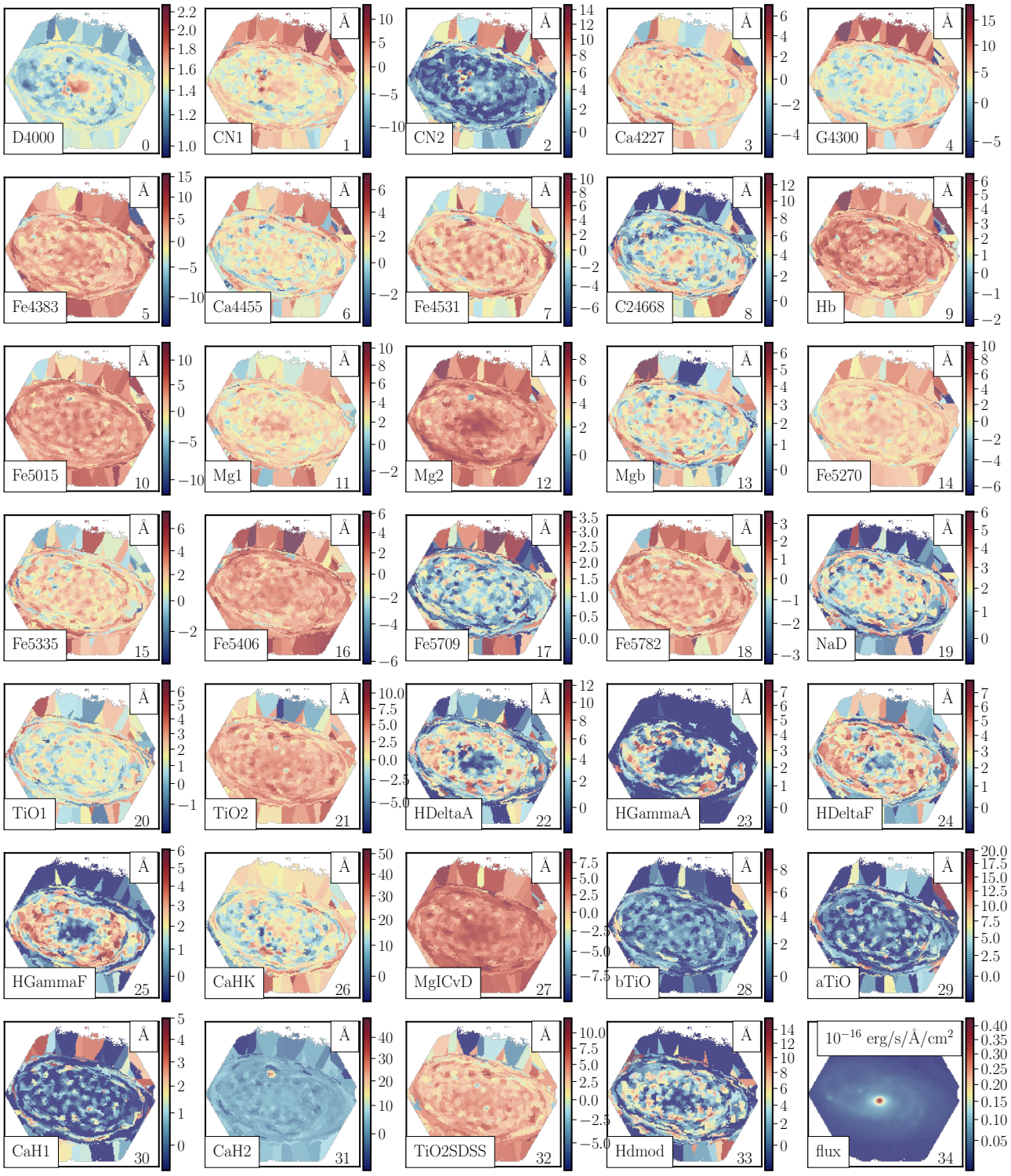

Fig. 3. Example of the content of the INDICES extension in the Pipe3D file, corresponding to the galaxy NGC2906. Each panel shows a color image with the content of a channel in this datacube. The actual content is indicated for each panel in the lower-left, the channel in the lower-right and the units of the represented quantity in the upper-right legend. For the flux and flux error the units are 10^{-16} erg/s/Å/cm^2. The colour figure can be viewed online.

TABLE 2

DESCRIPTION OF THE SSP EXTENSION

Channel	Units	Stellar index map
0	10^{-16} erg s^{-1} cm^{-2}	Unbinned flux intensity at ≈5500Å, f_V
1	none	Continuum segmentation index, CS
2	none	Dezonification parameter, DZ
3	10^{-16} erg s^{-1} cm^{-2}	Binned flux intensity at ≈5500Å, $f_{V,CS}$
4	10^{-16} erg s^{-1} cm^{-2}	StdDev of the flux at ≈5500Å, $ef_{V,CS}$
5	$\log_{10}$(yr)	Lum. weighted age, $\mathcal{A}_{\star,L}$, (log scale)
6	$\log_{10}$(yr)	Mass weighted age, $\mathcal{A}_{\star,M}$, (log scale)
7	$\log_{10}$(yr)	Error of both $\mathcal{A}_\star$, (log scale)
8	dex	Lum. weighted metallicity, $Z_{\star,L}$ in logarithmic scale, normalized to the solar value ($Z_\odot$ =0.017)
9	dex	Lum. weighted metallicity, $Z_{\star,M}$ in logarithmic scale, normalized to the solar value ($Z_\odot$ =0.017)
10	dex	Error of both $Z_\star$
11	mag	Dust extinction of the stellar pop., $A_{V,\star}$
12	mag	Error of $A_{V,\star}$, e_{A_V}
13	km/s	Velocity of the stellar pop., $vel_\star$
14	km/s	Error of the velocity, e_{vel}
15	km/s	Velocity dispersion of the stellar pop., $\sigma_\star$
16	km/s	Error of $\sigma_\star$, e_σ
17	$\log_{10}(M_\odot/L_\odot)$	Stellar mass-to-light ratio, $\Upsilon_\star$
18	$\log_{10}(M_\odot/sp^2)$	Stellar mass density per spaxel., $\Sigma_\star$
19	$\log_{10}(M_\odot/sp^2)$	Dust corrected $\Sigma_\star$, defined as $\Sigma_{\star,dust}$
20	$\log_{10}(M_\odot/sp^2)$	Error of $\Sigma_\star$

Channel indicates the Z-axis of the datacube starting from 0. (1) measured along the entire wavelength range covered by the spectroscopic data.

TABLE 3

DESCRIPTION OF THE SFH EXTENSION

Channel	Description of the map
0	$w_{\star,L}$ for ($\mathcal{A}_\star$,$Z_\star$) = (0.001 Gyr, 0.0001)
...	...
272	$w_{\star,L}$ for ($\mathcal{A}_\star$,$Z_\star$) = (13.5 Gyr, 0.04)
273	$w_{\star,L}$ for $\mathcal{A}_\star$ = 0.001 Gyr
...	...
311	$w_{\star,L}$ for $\mathcal{A}_\star$ = 13.5 Gyr
312	$w_{\star,L}$ for $Z_\star$ = 0.0001
...	...
318	$w_{\star,L}$ for $Z_\star$ = 0.04

Channel indicates the Z-axis of the datacube starting from 0, and $w_{\star,L}$ indicates the fraction (weight) of light at 5500Å corresponding to: (i) an SSP of a certain age ($\mathcal{A}_\star$) and metallicity (Z) (channels 0 to 272), (ii) a certain age, i.e., co-adding all $w_{\star,L}$ corresponding to SSPs with the same age but different metallicity (channels 273 to 311), and (iii) a certain metallicity, i.e., co-adding all $w_{\star,L}$ corresponding to SSPs with the same metallicity but different age (channels 312 to 318).

emission-line decontaminated spectra obtained as a by product of the analysis described in §3.1.2. This extension comprises the results from this analysis, including in each channel the values derived for each stellar index and the corresponding error. In this particular analysis we have updated the list of stellar indices previously included in the analysis by Pipe3D, comprising a total of 33 indices, whose actual definition and wavelength range were obtained from the compilation incorporated in the MaNGA Data Analysis Pipeline (Westfall et al. 2019)[11]. In addition we include the D4000 parameter as defined by Gorgas et al. (1999, their Eq. 2). We depart in this definition from the more usual one derived using the flux intensity in units of frequency (i.e., F_ν Bruzual A. 1983), as we find this former definition more convenient to work with. Table 4 describes the content of this extension, indicating the channel in which each stellar index and its corresponding error are stored. In addition, it includes the wavelength range defining the stellar index together with the blue and red wavelength ranges used to estimate the adjacent continuum. Finally, we illustrate the content of this extension in Figure 3, showing the stellar indices derived for the galaxy NGC 2906. Note how some stellar indices sensitive to the $\mathcal{A}_\star$ ($\mathcal{Z}_\star$) like D4000 (Mg2 or Mgb) present a negative gradient from the inside-out, while other indices more sensitive to the presence of young stellar populations (e.g., HdeltaA o or Hb) present a clear increase near the location of the spiral arms (i.e., where the younger stellar populations are found).

[11] https://www.sdss4.org/dr17/manga/manga-analysis-pipeline/

TABLE 4

DESCRIPTION OF THE INDICES EXTENSION

ID	Channel	Units	Index λ range (Å)	Blue λ range (Å)	Red λ range (Å)
D4000	0/35	Å	4050.000-4250.000	3750.000-3950.000	
CN1	1/36	Å	4142.125-4177.125	4080.125-4117.625	4244.125-4284.125
CN2	2/37	Å	4142.125-4177.125	4083.875-4096.375	4244.125-4284.125
Ca4227	3/38	Å	4222.250-4234.750	4211.000-4219.750	4241.000-4251.000
G4300	4/39	Å	4281.375-4316.375	4266.375-4282.625	4318.875-4335.125
Fe4383	5/40	Å	4369.125-4420.375	4359.125-4370.375	4442.875-4455.375
Ca4455	6/41	Å	4452.125-4474.625	4445.875-4454.625	4477.125-4492.125
Fe4531	7/42	Å	4514.250-4559.250	4504.250-4514.250	4560.500-4579.250
C24668	8/43	Å	4634.000-4720.250	4611.500-4630.250	4742.750-4756.500
Hb	9/44	Å	4847.875-4876.625	4827.875-4847.875	4876.625-4891.625
Fe5015	10/45	Å	4977.750-5054.000	4946.500-4977.750	5054.000-5065.250
Mg1	11/46	Å	5069.125-5134.125	4895.125-4957.625	5301.125-5366.125
Mg2	12/47	Å	5154.125-5196.625	4895.125-4957.625	5301.125-5366.125
Mgb	13/48	Å	5160.125-5192.625	5142.625-5161.375	5191.375-5206.375
Fe5270	14/49	Å	5245.650-5285.650	5233.150-5248.150	5285.650-5318.150
Fe5335	15/50	Å	5312.125-5352.125	5304.625-5315.875	5353.375-5363.375
Fe5406	16/51	Å	5387.500-5415.000	5376.250-5387.500	5415.000-5425.000
Fe5709	17/52	Å	5696.625-5720.375	5672.875-5696.625	5722.875-5736.625
Fe5782	18/53	Å	5776.625-5796.625	5765.375-5775.375	5797.875-5811.625
NaD	19/54	Å	5876.875-5909.375	5860.625-5875.625	5922.125-5948.125
TiO	20/55	Å	5936.625-5994.125	5816.625-5849.125	6038.625-6103.625
TiO2	21/56	Å	6189.625-6272.125	6066.625-6141.625	6372.625-6415.125
HDeltaA	22/57	Å	4083.500-4122.250	4041.600-4079.750	4128.500-4161.000
HGammaA	23/58	Å	4319.750-4363.500	4283.500-4319.750	4367.250-4419.750
HDeltaF	34/59	Å	4091.000-4112.250	4057.250-4088.500	4114.750-4137.250
HGammaF	25/60	Å	4331.250-4352.250	4283.500-4319.750	4354.750-4384.750
CaHK	26/61	Å	3899.500-4003.500	3806.500-3833.800	4020.700-4052.400
MgICvD	27/62	Å	5165.000-5220.000	5125.000-5165.000	5220.000-5260.000
bTiO	28/63	Å	4758.500-4800.000	4742.750-4756.500	4827.875-4847.875
aTiO	29/64	Å	5445.000-5600.000	5420.000-5442.000	5630.000-5655.000
CaH1	30/65	Å	6357.500-6401.750	6342.125-6356.500	6408.500-6429.750
CaH2	31/66	Å	6775.000-6900.000	6510.000-6539.250	7017.000-7064.000
TiO2SDSS	32/67	Å	6189.625-6272.125	6066.625-6141.625	6422.000-6455.000
Hdmod	33/68	Å	4083.500-4122.250	4079.000-4083.000	4128.500-4161.000
SN	34/69	10^{-16}cgs	Signal/Error across the entire wavelength range		

Channel indicates the Z-axis of the datacube starting from 0.

4.1.4. *ELINES extension*

As described in §3.1.3 the emission lines were analyzed using two different methods. In the first one a set of strong emission lines were modelled with a Gaussian function. The spatial results of this analysis are included in the ELINES extension, whose content is described in Table 5. The information provided in this table is stored in a set of header keywords, DESC_N, with N being the channel number. Figure 4 shows an example of the content included in this extension corresponding to the analysis on the galaxy NGC 2906. The first channel, that comprises the Hα velocity map, shows a typical rotational pattern for a spiral galaxy. The pattern is visible for those regions with clear detection of the ionized gas (e.g., in Hα, 7th channel). For all emission lines the ionized gas intensity maps present a clumpy structure tracing the lo-

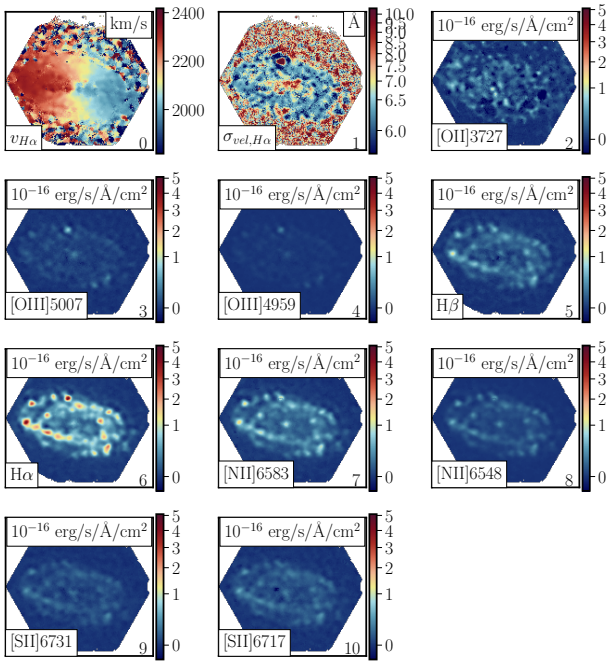

Fig. 4. Example of the content of the ELINES extension in the Pipe3D file, corresponding to the galaxy NGC2906. Each panel shows a color image with the content of a channel in this data cube. The first panel corresponds to the velocity, in km/s, and the 2nd panel to EW(Hα), in Å. The remaining panels represent the distribution of the flux intensities for the different analyzed emission lines (lower-left legend), in units of 10^{-16} erg/s/Å/cm^2. The color figure can be viewed online.

TABLE 5

DESCRIPTION OF THE ELINES EXTENSIONS

Channel	Units	Description of the map
0	km/s	Hα velocity
1	Å	Hα velocity dispersion[a]
2	10^{-16} erg s^{-1} cm^{-2}	[OII]3727 flux intensity
3	10^{-16} erg s^{-1} cm^{-2}	[OIII]5007 flux intensity
4	10^{-16} erg s^{-1} cm^{-2}	[OIII]4959 flux intensity
5	10^{-16} erg s^{-1} cm^{-2}	Hβ flux intensity
6	10^{-16} erg s^{-1} cm^{-2}	Hα flux intensity
7	10^{-16} erg s^{-1} cm^{-2}	[NII]6583 flux intensity
8	10^{-16} erg s^{-1} cm^{-2}	[NII]6548 flux intensity
9	10^{-16} erg s^{-1} cm^{-2}	[SII]6731 flux intensity
10	10^{-16} erg s^{-1} cm^{-2}	[SII]6717 flux intensity

Channel indicates the Z-axis of the data cube starting from 0. [a] FWHM, i.e., 2.354σ. The instrumental velocity dispersion has not been removed.

TABLE 6

DESCRIPTION OF THE FLUX_ELINES EXTENSIONS

Channel	Units	Description of the map
I	10^{-16} erg s^{-1} cm^{-2}	Flux intensity
I+N	km/s	Velocity
I+2N	Å	Velocity dispersion FWHM
I+3N	Å	Equivalent width
I+4N	10^{-16} erg s^{-1} cm^{-2}	Flux error
I+5N	km/s	Velocity error
I+6N	Å	Velocity dispersion error
I+7N	Å	Equivalent width error

I is the index that identifies each of the analyzed emission lines, running from 0 to N, where N is the total number of analyzed emission lines: (i) 53 for the FLUX_ELINES extension and (ii) 130 for the FLUX_ELINES_LONG one.

cation of the H II regions and clusters, which is the typical distribution for this kind of galaxies (e.g., Sánchez 2020; Sánchez et al. 2021).

4.1.5. *FLUX_ELINES and FLUX_ELINES_LONG Extensions*

In addition to the Gaussian modelling the emission parameters are estimated using a moment analysis, as described in §3.1.3. This second analysis is performed twice, using two different list of emission lines, and the results are stored in two different extensions of the pyPipe3D data file: (i) the 53 emission lines included in original version of the Pipe3D pipeline (Sánchez et al. 2016b, Table 1, limited to λ <7400Å), included in the FLUX_ELINES extension, and (ii) a new set of 130 emission lines extracted from the list published by Fesen & Hurford (1996), covering the wavelength range between 3700Å and 7200Å, in the rest-frame, included in the FLUX_ELINES_LONG extension. Details about this new list of emission lines are included in Appendix A.

Table 6 describes the format of both extensions. For each analyzed emission line (defined by the running index I), the extension comprises four different parameters (flux intensity, velocity, velocity dispersion and equivalent width) and their corresponding errors. Thus, a total of eight channels, from I to I+7N, correspond to the N different parameters derived for the same I emission line, with 0≤ N <8 and I running from 0 to 53 (130) for the FLUX_ELINES (FLUX_ELINES_LONG) extension.

Figure 5 shows an example of the content of these extensions, corresponding to the four parameters derived for the Hα emission line, and their associated errors, stored in the FLUX_ELINES extension of the galaxy

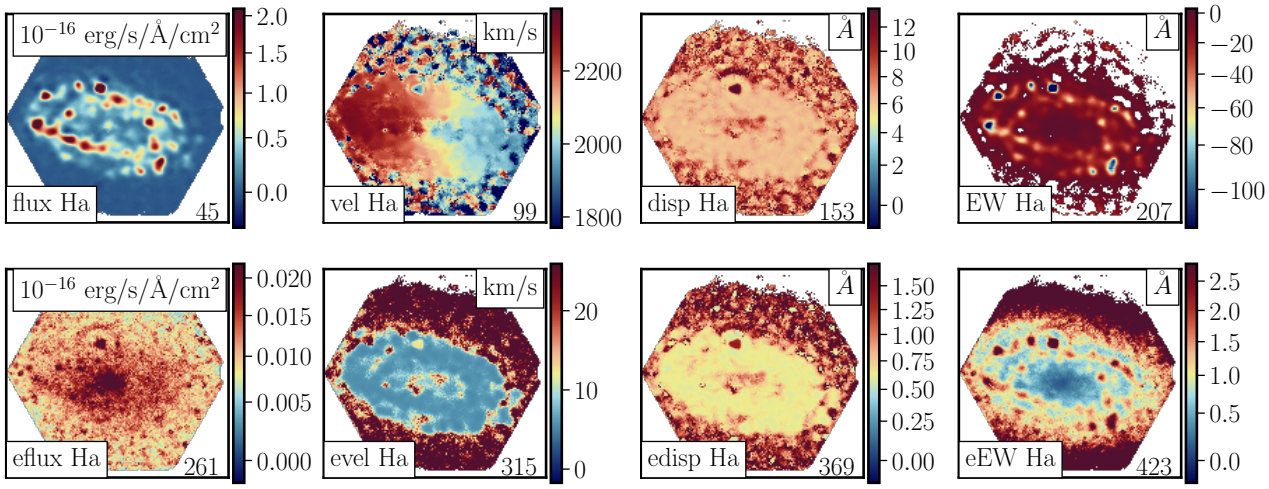

Fig. 5. Example of the content of the FLUX_ELINES extension in the Pipe3D file, corresponding to the galaxy NGC2906. Each panel shows a color image with the content of a channel in this datacube. For each panel, the actual content is indicated in the lower-left, the channel number in the lower-right, and the units of the represented quantity in the upper-right legend. For the flux and flux error the units are 10^{-16} erg/s/Å/cm^2. The color figure can be viewed online.

NGC 2906. As expected the distributions observed in the flux intensity, velocity and velocity dispersion maps are very similar to those already seen in Figure 4, corresponding to the same emission line derived adopting a Gaussian model. Finally, the EW(Hα) map presents a clumpy pattern that follows the intensity distribution, with clear negative values at the location of the H II regions. Much lower values, near to 3Å or below (in absolute values) are found at the locations where the ionized gas presents a more smooth distribution, being compatible with a diffuse ionized gas dominated by hot evolved/post-AGB stars (see §4 of Sánchez et al. 2021, for a more clear description of this distribution).

As a final remark, we should highlight that in both the ELINES and FLUX_ELINES extensions the distributed velocity dispersion corresponds to the FWHM of the emission lines measured in units of Å. Furthermore, the instrumental dispersion is not subtracted. As described in Sánchez et al. (2022) it is needed to apply the following formula to estimate the velocity dispersion in km s^{-1}:

$$\sigma_{\text{Å}} = \text{FWHM}/2.354, \quad \sigma_{\text{kms}^{-1}} = \frac{c}{\lambda}\sqrt{\sigma^2_{\text{Å}} - \sigma^2_{\text{inst}}}, \quad (9)$$

where c is the speed of light in km s^{-1}, λ is the wavelength of the emission line and σ_{inst} is the instrumental resolution (≈2.6Å).

4.1.6. *GAIA_MASK Extension SELECT_REG Extension*

These two extensions comprise the results of the two masking processes described in §3.2: GAIA_MASK includes the mask of the foreground stars identified using the Gaia DR3 catalog, while SELECT_REG includes the mask generated using the signal-to-noise distribution for the continuum, by selecting a minimum value of S/N>1. The S/N ratio was derived by estimating the flux intensity and standard deviation for each individual spectrum within the wavelength range between 5589 and 5680 Å. Although the main shape of the continuum is removed, the absorption features remain. Therefore, this S/N is an lower limit to the real one.

4.2. *Catalog of Individual Parameters*

As described in §3.4, following Sánchez et al. (2022), we derive a set of individual parameters for each galaxy, comprising both integrated, aperture limited and characteristics parameters (i.e., values at the effective radius), and, for a subset of them, the slopes of their radial gradients. For doing so we use the information included in each individual `pyPipe3D` file described in §4.1, and the calculations described in §3.3. The final parameter set is distributed as a catalog and described in Appendix B.

4.3. *NGC 2906: A Show-Case Galaxy*

Along the previous sections we have used the galaxy NGC 2906 as a show case to illustrate the content of each of the extensions in the distributed `pyPipe3D` files. NGC 2906 is a rotational supported Sbc galaxy with a stellar mass similar to that of the Milky-Way (≈10^{10}M$_\odot$), being a star-forming galaxy located within 1σ of the star-formation main sequence, and possibly hosting a weak AGN (e.g. Angthopo et al. 2022). Furthermore, it

presents a well defined bulge and two clearly distinguishable spiral arms. With these properties it can be considered an archetype late-type galaxy, suitable to illustrate the content of the distributed data products. NGC 2906 was observed by the CALIFA survey on 17th December 2012. Later on, it was observed during the science verification of the MUSE instrument, being included in the AMUSING++ compilation (López-Cobá et al. 2020). Therefore, it is also a suitable target to explore the improvement of spatial resolution introduced by the new reduction.

4.3.1. *NGC 2906: Resolved Properties of the Ionized Gas*

We already mentioned that one of the major improvements of the new analyzed and distributed data set is the increased spatial resolution. The previous reduction provides a spatial resolution that on average is of the order of ≈2.5″/FWHM (version 2.2; Sánchez et al. 2016a). For the particular case of NGC 2906, this FWHM was estimated as 2.37″, according to the information provided by the data reduction stored in the datacube header. The new reduction improves the spatial resolution with a final PSF FWHM near to the one provided by the natural seeing (Sanchez et al. 2023). In the particular case of NGC 2906 is estimated as 1.1″/FWHM. When considering the offset between the PSF FWHM estimated by the data-reduction itself and the real FWHM of the natural seeing (Sanchez et al. 2023), a more realistic estimation would be ≈1.5″. This is, in any case, a very significant improvement in the spatial resolution with respect to the previous data reduction.

A clear advantage of an improved spatial resolution is the ability to distinguish between different structures within a galaxy. This is particularly important, for instance, in the exploration of the different ionizing sources and the understanding of the changes in the physical conditions of the inter-stellar medium (ISM) across the optical extension of galaxies. This has been highlighted in recent reviews on the topic (Sánchez 2020; Sánchez et al. 2021), and the results by recent projects aimed to explore the ionizing conditions using IFS with unprecedented spatial resolutions (e.g., PHANGS-MUSE; Emsellem et al. 2022).

Figure 6 shows a comparison between the spatial distribution of the continuum emission, created using the $u-$, $g-$ and $r-$band images synthetized from the reduced eCALIFA data cube, dominated by the stellar population (panel a), and the ionized gas emission lines, created using the [O III] (blue), Hα (green) and [N II] (red) emission maps (panel b). The different morphological structures within this galaxy are clearly appreciated in the contin-

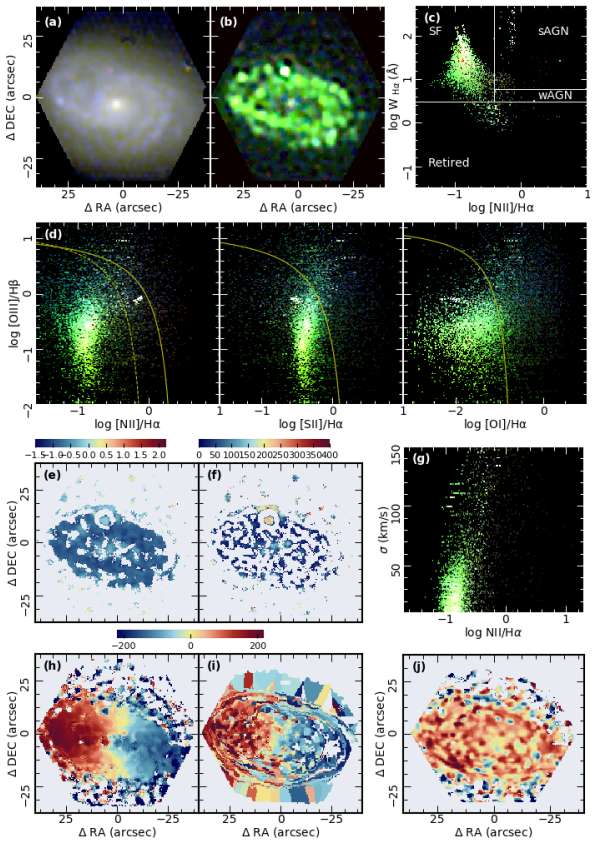

Fig. 6. Example of the information explored in the quality control process for the galaxy/cube NGC2906, extracted from the analysis presented by López-Cobá et al. (2020). Each panel comprises the following information: (a) RGB three-color image created using the $u-$, $g-$ and r-band images synthetized from the reduced eCALIFA data cubes; (b) RGB color image created using the [O III] (blue), Hα (green), and [N II] (red) intensity maps estimated by `pyPipe3D`; (c) spatially resolved WHAN diagnostic diagram, with each spaxel color-coded using the color-scheme shown in panel (b). The white solid lines indicate the boundaries proposed by Cid Fernandes et al. (2011), with the dominant ionizing source in each region included as labels; (d) spatially resolved diagnostic diagrams showing the distribution of [OIII]/Hβ as a function of [NII]/Hα, [SII]/Hα and [OI]/Hα, using a similar color scheme as panel (c) (Baldwin et al. 1981; Veilleux et al. 2001). The yellow solid and dashed lines in each panel correspond to the demarcation line proposed to separate between SF and non-SF dominated ionization by Kewley et al. (2001) and Kauffmann et al. (2003), respectively; (e) spatial distribution of the [NII]/Hα line ratio; (f) spatial distribution of the Hα velocity dispersion; (g) distribution of the [NII]/Hα line ratio as a function of the Hα velocity dispersion across the extension of the galaxy; (h) Hα velocity map (spaxel-wise); (i) stellar population velocity map (following the spatial-binning/tessallation); (j) difference between velocity maps shown in panels (h) and (i) . Note that the scale of this later panel is not the same as those in panel (h) and (i). The color figure can be viewed online.

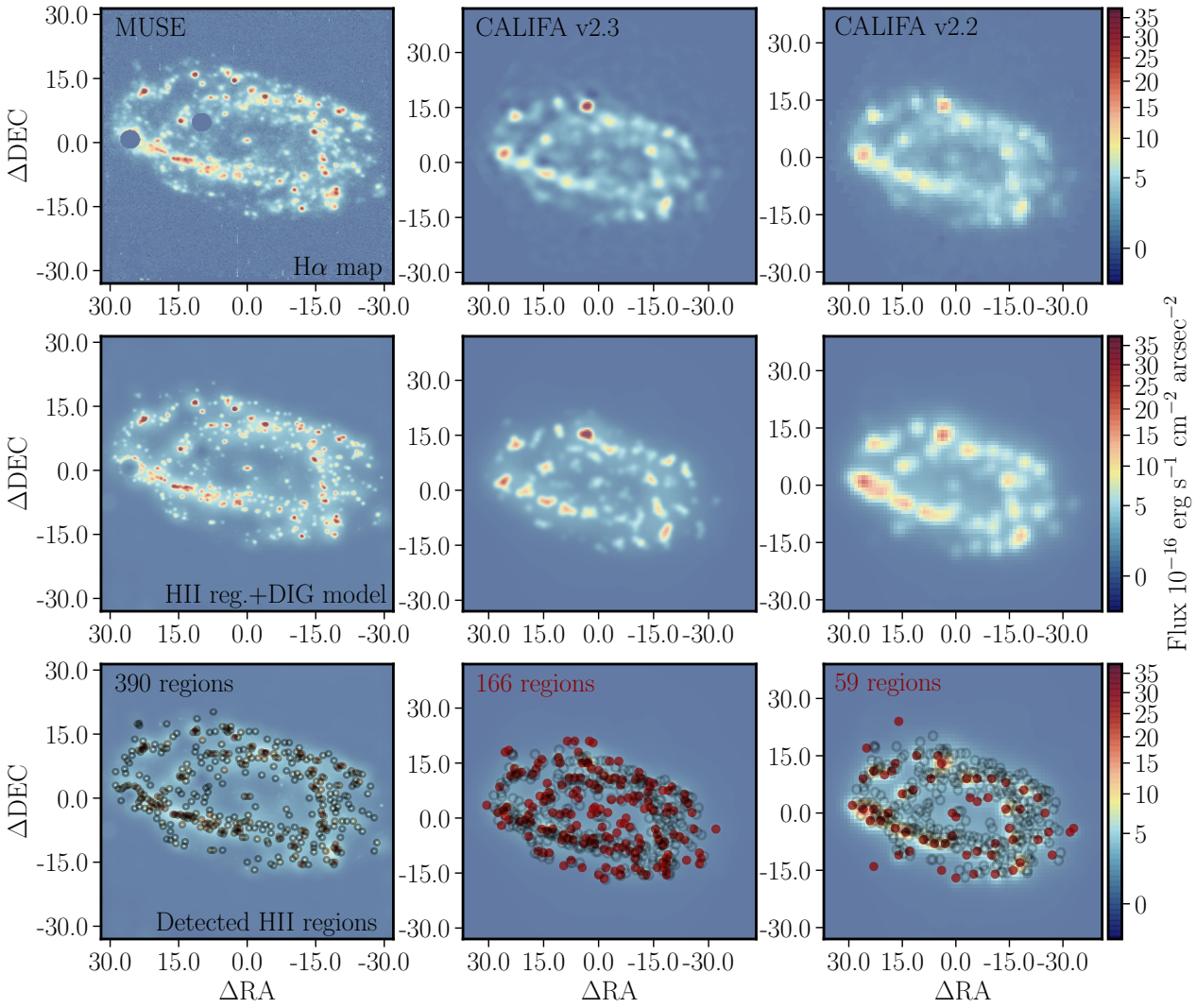

Fig. 7. Hα intensity maps of NGC 2906 extracted using `pyPipe3D` from (i) the MUSE data cube included in the AMUSING++ compilation (López-Cobá et al. 2020) (top-left panel), (ii) the eCALIFA data cube corresponding to version 2.3 of the data reduction Sanchez et al. (2023)(top-central panel), and (iii) the CALIFA data cube corresponding to version 2.2 of the data reduction (top-right panel). The best models for the H II regions and diffuse ionized gas recovered by `pyHIIExtractor` (Lugo-Aranda et al. 2022) for each of those maps shown in the top panels are included in the middle panels, following the same sequence from left-to-right (MUSE, eCALIFA v2.3 and v2.2). Finally, the bottom panels show each of these models together with the distribution of good-quality H II regions detected using the MUSE data (black open-circles, included in all the bottom panels), and the regions detected using each of the eCALIFA data (solid red-circles). The number of H II regions detected using each dataset is included in a label in each of the bottom panels. The figure illustrates the effects of the degradation of the spatial resolution in the detectability of individual structures (e.g., H II regions) in galaxies using this kind of data. The color figure can be viewed online.

uum image: (i) an evident (but small) bulge is observed in the center of the galaxy, clearly dominated by a red/old stellar population; (ii) two spiral arms, with some additional sub-arms, are traced by a blue/young stellar component; in addition, (iii), a diffuse component dominated by reddish/oldish stellar populations is appreciated beyond and in between the spiral arms. The ionized gas map is dominated by a clumpy structure, mostly green (i.e., with a dominant Hα flux over the other two emission lines), that traces the location of the spiral arms seen in the continuum image (i.e., associated with the presence of a blue/young stellar population).

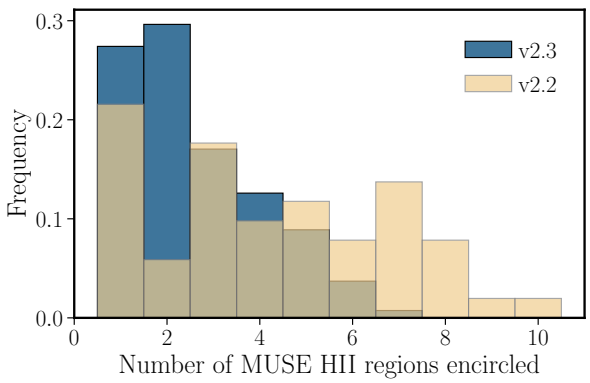

Fig. 8. Distribution of the frequency in which a certain number of H II regions detected using the MUSE data shown in Figure 7 is encircled within the radius of an H II region detected using the eCALIFA v2.3 dataset (blue histogram) or the v2.2 one (yellow histogram). Figure illustrates the effect of the degradation of the spatial resolution in the clustering of H II regions into a single blended structure. The color figure can be viewed online.

These clumps are most probably tracing H II regions/clusters. This is evident when explored their distribution in the different diagnostics diagrams included in Figure 6, panels (c) and (d). The vast majority of them are found in regions within the diagnostic diagrams usually associated with classical H II regions (e.g. Osterbrock 1989; Kewley et al. 2001; Kauffmann et al. 2003) or regions in which ionization is associated with recent star-formation activity (e.g. Cid Fernandes et al. 2011), in agreement with the prescriptions outlined by Sánchez et al. (2021). Besides those clumps there is a smooth/diffuse component that is observed at any location within the galaxy, including the central regions and inter-arms, that most probably is due to a combination of different ionizing sources, such as photons leaked from H II regions and ionization due to the presence of hot evolved/post-AGB stars (e.g. Binette et al. 1994; Relaño et al. 2012; Singh et al. 2013; Weilbacher et al. 2018; Sánchez et al. 2021; Belfiore et al. 2022). Finally, this object is a known host of a supernova remnant (SNR; Martínez-Rodríguez in prep.) located at ≈10″ north and ≈2″ east from the center of the galaxy. This SNR is observed as a white-roundish ionized structure in panel (b), and as a cluster of white points in the intermediate region[12] in the [O III]/Hβ vs [N II]/Hα diagram (BPT diagram; Baldwin et al. 1981), included in panel (b).

Figure 6, panel (e) shows the spatial distribution of the N2 parameter, defined as log([N II]/Hα). This parameter is sensitive to oxygen abundance when the ionization is due to young OB-stars (e.g. Pettini & Pagel 2004; Marino et al. 2013). A mild negative gradient is observed, with values of N2 slightly larger in the central regions than in the outskirts, compatible with the known decline of the oxygen abundance described for galaxies of this stellar mass and morphology (e.g., Sánchez et al. 2014; Belfiore et al. 2017b; Sánchez et al. 2021; Boardman et al. 2023). Those regions ionized by other sources, different than young massive stars, usually present larger values of N2. This is the reason why this parameter is used to discriminate the ionizing source in the WHAN diagram (panel c). In this particular galaxy we find anomalous large values of the N2 ratio compared to those at the same galactocentric distances at the location of the reported SNR (e.g., Cid Fernandes et al. 2021). We stress that this N2-enhancement is a direct consequence of an extra ionizing source, and should never be considered as an increase of the oxygen abundance.

If we compare the N2 distribution with the one shown in panel (f), the Hα velocity dispersion, we can appreciate that there is an increase of this parameter at the location of the SNR too. As we indicated before the spectral resolution of these data is not optimal to measure the velocity dispersion, in particular in the disk of late-type spirals, where this parameter is expected to be well below the instrumental resolution. This is the reason why in many locations across the extension of this galaxy the velocity dispersion is masked. For those regions for which a reliable estimation is obtained we appreciate that a decline in the velocity dispersion from a value near ≈150 km s^{-1} in the central regions to values as low as ≈30 km s^{-1}, in the outer disk. However, at the location of the SNR the velocity dispersion rises up to ≈200 km s^{-1}. Recent explorations have proposed that the velocity dispersion should be considered as an extra parameter to discriminate between different ionizing sources (D'Agostino et al. 2019; López-Cobá et al. 2020; Law et al. 2021). Indeed, the N2 parameter usually follows the velocity dispersion, as appreciated in panel (g) of Figure 6. Due to their association with the gas disk and their relatively low internal pressure H II/SF regions are usually associated with regions of low velocity dispersion (e.g. Law et al. 2021). On the contrary, regions ionized by shocks present larger velocity dispersions (e.g. D'Agostino et al. 2019; López-Cobá et al. 2020).

The last three panels of Figure 6 show the Hα and stellar velocity maps (panels h and i), and finally the difference between both of them (panel j). The well defined rotational pattern appreciated in both velocity maps, together with the low velocity dispersion seen in panel (f), suggests that this is a rotationally supported galaxy. A possible perturbation on the rotational pattern is appreciated in the inner regions of the Hα velocity map, although a more detailed analysis would be required to

[12] In between the Kewley et al. (2001) and Kauffmann et al. (2003) demarcation lines in the diagnostic diagram

drawn any conclusion in this regards, which is beyond the scope of the current analysis. Apart from a general offset, there is no discernible pattern in the difference between both velocity maps. The nature of the offset is a known effect in the calibration of the zero-velocity associated with the measurements using an SSP template, a mismatch that we have already reported in previous articles (e.g. Sánchez et al. 2022), that it is associated with the definition of the central wavelength at the edge or at center of the spectral pixel. It produces an offset of half of the spectral pixel (in velocities), times the expansion factor introduced by the redshift, i.e., $1+z$. This offset should be corrected prior to any detailed comparison between the two velocity maps (for all the delivered data sets). A more detailed exploration, matching the offset in velocity in the central regions, is required to explore possible patterns associated with known effects, such as the asymmetric drift or the possible presence of non-radial motions that may affect differently the gas and the stellar populations. Like in the case of the N2 and velocity dispersion maps the strongest deviation appreciated in the gas velocity maps is at the location of the SNR, where a clear blue-shift is observed. These asymmetries or multiple kinematic components are frequent in the presence of shock ionization (e.g. Veilleux et al. 2001; López-Cobá et al. 2017).

4.3.2. *NGC 2906: Ability to Segretate* H II *Regions*

The content of Figure 6, together with the distributions shown in Figures 1 to 5 clearly illustrate the kind of information extracted by `pyPipe3D` from the new reduced data cubes. It also shows in a qualitative way how the new spatial resolution allows to distinguish between different structures within the galaxy. In this section we present a more quantitative statement of this improvement, by comparing the ability to detect and segregate H II regions (and associations) using three IFS data sets on the galaxy NGC 2906: (i) the MUSE data analyzed by Pipe3D as part of the AMUSING++ compilation (López-Cobá et al. 2020); (ii) the eCALIFA v2.3 data analyzed by `pyPipe3D` discussed in this article and (iii) the CALIFA v2.2 data analyzed by `pyPipe3D` distributed as part of the DR3 (Sánchez et al. 2016a).

Figure 7, top panels, show the Hα intensity map extracted from the three data sets. As expected the MUSE data present the richest content of sub-structures/clumpy regions (i.e., H II regions), due to its better spatial resolution (FWHM$\approx$0.6″). In comparison, the eCALIFA v2.3 data (FWHM$\approx$1.1-1.5″) still traces the brightest clumpy structures seen in the MUSE data. However, they present a clear degradation of the image quality, bluring and/or grouping into a single structure several clumps clearly visible and/or segregated in the MUSE data. Finally, the lowest number of substructures is appreciated in the CALIFA v2.2 data (FWHM$\approx$2.37″), with the largest degree of clumpy regions lost or grouped into a single unresolved or barely resolved structure.

To quantify these differences we apply the recently developed `pyHIIExtractor` code (Lugo-Aranda et al. 2022) to the three data sets. This code comprises an algorithm that detects clumpy regions in emission line maps, deriving both their flux intensities and sizes. It also segragates the detected regions from the diffuse ionized gas (DIG), generating a model for both components. Being developed to explore the H II regions of the galaxies within the AMUSING++ compilation (Lugo Aranda et al., in prep.), its capabilities have been tested with a wide range of simulations. Figure 7, middle-column panels, show the combined models (H II regions+DIG) generated by this code when applied to the Hα maps shown in the upper panels, using the same input parameters: (i) a minimum size of 30 pc ($\approx$0.6″ at the redshift of the object), (ii) a maximum size of 300 pc, (iii) a overall detection limit of 3σ, and (iv) a minimum contrast of a 50% with respect to the DIG in the detection of a clumpy structure. A direct comparison between the upper and middle-column panels illustrates how well the code recovers the original light distribution. It also highlights its limits: it is unable to recover some of the faintest/smaller clumpy regions in the MUSE data. We should note that the most limiting factor is the contrast with respect to the level of the adjacent DIG, followed by the imposed minimum size.

The three bottom panels in Figure 7 show again the same Hα models, together with the distribution of clumpy structures detected by `pyHIIExtractor` using the MUSE data, that is repeated in the three panels for comparison purposes. In addition, it is shown the distribution of regions detected by this code using the eCALIFA v2.3 (central panel), and CALIFA v.2.2 (right panel), respectively. In the case of the MUSE data a total of 390 clumpy regions is detected, a number that decreases to 166 for the eCALIFA v2.3 data and to just 59 for the CALIFA v2.2 data, respectively. Thus, the resolution clearly affects the ability to detect individual structures such as H II regions. Furthermore the new reduced and analyzed data set presents a clear improvement with respect to the previous data set.

As discussed previously, H II regions are lost due to the bluring effect introduced by the degradation of the resolution (i.e., they are not distinguished from the background), but also due to an aggregation with nearby clumps. To quantify both effects we determine how many of the detected regions in the MUSE data are not included within the radius of the clumpy structures detected in the other two data sets. This will tell us the number of regions

that are totally lost. Finally, we determine the number of regions detected in the MUSE encircled within the radius of the regions detected using the other two data sets. This will quantify the frequency with which an original region is aggregated to form a new structure in the lower resolution datasets. To do so we make use of the `cKDthree` algorithm included in the `scipy.spatial` python package to look for the nearest neighbours of each of the regions detected in the MUSE data in the catalog of regions derived using the other two data sets. Then, we determine whether a region is included within any nearest neighbor by comparing their radii with the distance.

Of the 390 regions detected in the MUSE data, 351 are included within one of the 166 regions detected in the eCALIFA data. Thus, most of the regions are not really lost (≈90%), but they are rather aggregated into larger clumps, that on average comprise ≈2 of the former regions. On the contrary, in the case of the CALIFA v2.2 data, only 218 of the original 390 regions are included within one of the detected 59 regions. Therefore, the "recovery" rate is much lower (≈55%). Furthermore, the new clumps comprise a larger number of the original regions (≈3-4). Therefore, the improved resolution achieved by the new reduction increases the recovery rate of H II regions and decreases the number of agregated/grouped regions by a factor of two. A more detailed exploration on how the original H II regions are aggregated into larger structures is presented in Figure 8, where is shown the frequency at which a certain number of the former regions is aggregated to a region detected in the other data sets. In the case of the eCALIFA v2.3 data set most of the detected regions comprise one or two MUSE-detected regions (≈60%), with less than ≈20% encircling more than four of those regions. On the contrary, in the case of the CALIFA v2.2 data, only ≈25% of the regions comprise one or two MUSE-detected regions, while more than ≈50% aggregates more than four of those regions.

In summary, this exploration clearly indicates that the new reduced and analyzed data have significantly improved out the ability to detect and study sub-structures in the observed galaxies.

4.4. *Ionization Conditions Across the Optical Extension of Galaxies*

In previous sections we have illutrated the impact of the intrinsic properties of the data (i.e., spatial coverage and sampling) and the improved spatial resolution of the new reduced data set, on the exploration of the ionizing conditions and ISM properties in one particular galaxy NGC 2906. In this section we illustrate their impact on the exploration of the general patterns of those properties described for the full population of galaxies. To do so we replicate the explorations presented by Sánchez (2020) and Sánchez et al. (2022), shown in their Figure 5 and Figure 10, respectively. There it was presented the spaxel-wise spatial resolved distribution of values across the classical BPT diagnostic diagram, [OIII]/Hβ vs. [NII]/Hα (BPT; Baldwin et al. 1981) for two different samples of galaxies, segregated by stellar mass and morphology. In both cases it was claimed that the selected samples were representative of the galaxy population in the nearby Universe: (i) Sánchez (2020) explored an heterogeneous compilation of galaxies observed using different IFS instruments by different surveys, and (ii) Sánchez et al. (2022) used the final DR of the MaNGA IFS galaxy survey.

Following both studies we select a refined sub-sample of 660 galaxies from the original data set, excluding edge-on galaxies (a/b >0.85), galaxies poorly resolved (Re<2″), and limiting the redshift range (0.005< z <0.05). This way we (i) avoid projection issues, providing a cleaner interpretation of the galactocentric distances, (ii) exclude galaxies that are not resolved by the data, and (iii) limit the effects of the wide range of physical resolutions (≈500 pc, on average, ranging from 150 pc to 1 kpc) in the interpretation of the results. We should highlight that this selection biases the sample excluding (i) the most prominent/evident galactic outflows, shock ionized and frequently observed as biconical, cononical or filamentary structures of gas extending along the vertical axis in edge-on galaxies (e.g. Bland-Hawthorn 1995; Heckman et al. 1990; López-Cobá et al. 2020); and (ii) the weak extra-planar diffuse ionized gas that is observed as part of the thick disk in some edge-on galaxies too (e.g. Flores-Fajardo et al. 2011; Levy et al. 2018).

For each galaxy we obtain the distribution of the average EW(Hα) and the density of spaxels across the considered BPT diagram. Then, for the full sample and for any sub-sample selected by stellar mass and/or morphology, we average both distributions. This way each ionized spaxel and each galaxy weighs the same, irrespectively of the flux intensity of the emission lines. Therefore, by construction the possible contribution of strong but spatially concentrated ionizing sources, like AGNs, is somehow diluted. Together with the bias against strong shock ionized structures, we acknowledge that most of the patterns that emerge from this exploration are related to the dominant (in terms of spatial extent) ionizing sources in galaxies: i.e., stars.

Figure 9 shows, for each panel, the average distributions along the BPT diagram for a different subset of galaxies. Top-left panel includes the diagram for the full sub-sample. Then, each column corresponds to galaxies of different morphologies: (i) early-type galaxies (E/S0), (ii) early-spirals or spirals with prominent bulge (Sa/Sb),

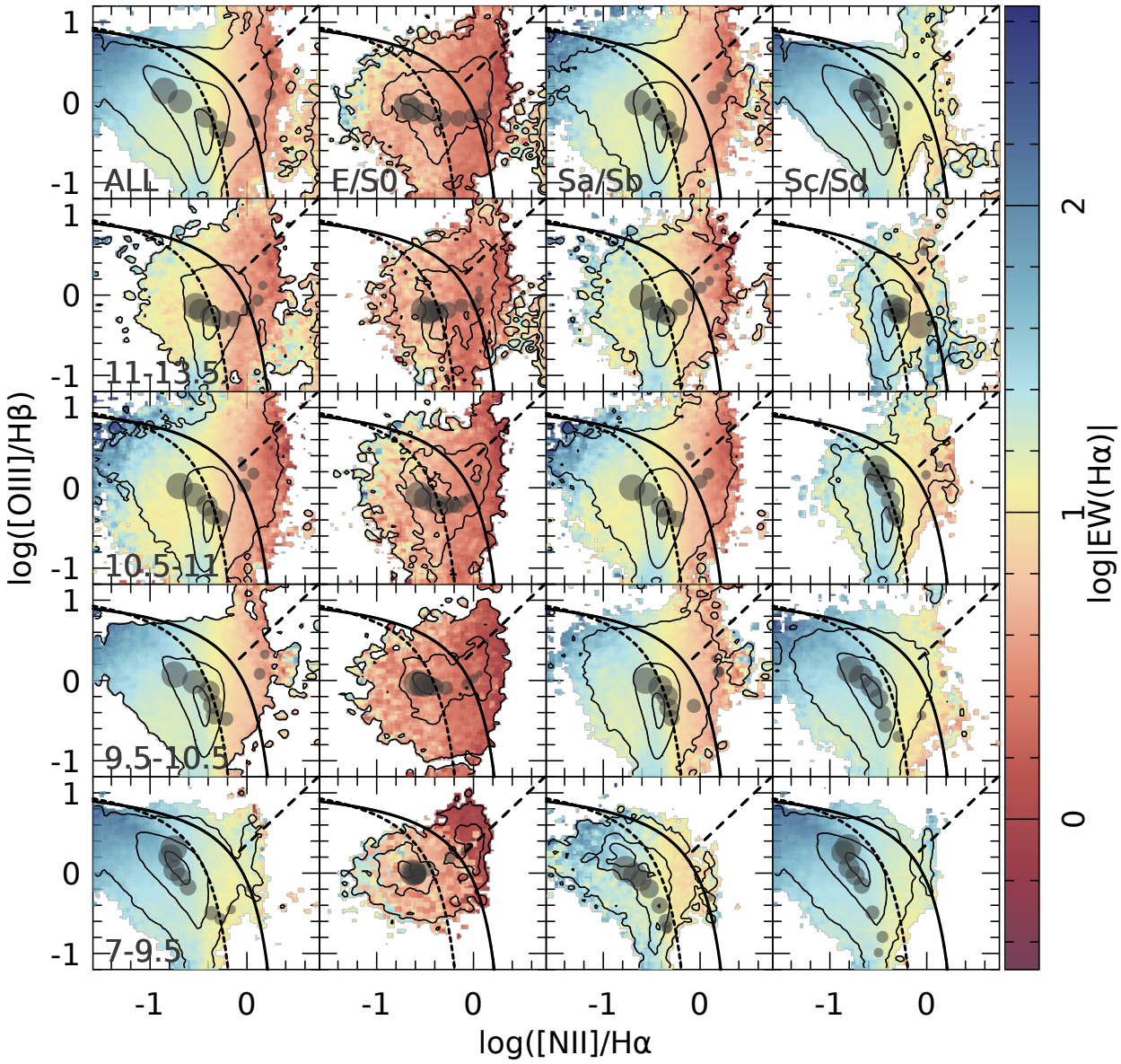

Fig. 9. EW(Hα) across the classical [OIII/Hβ] vs. [NII]/Hα BPT diagram (Baldwin et al. 1981) for ≈9 million individual spaxels extracted from a sub-sample of 660 face-on (a/b <0.85), well resolved (Re>2″) and redshift limited (0.005< z <0.05) galaxies. Each panel shows the distribution for a sub-set of galaxies with different morphologies (columns) and stellar masses (rows), and the top-left panel includes the complete sub-sample, using the same symbols and color schemes: (i) the density of spaxels is traced by the successive contours encircling 90, 50 and 10% of the individual points; (ii) the average values at different galactocentric distances, ranging from 0.1 to 2.1 Re (ΔRe=0.2), are represented by the grey circles, whose size increases with the distance; (iii) the classical demarcation lines defined by Kewley et al. (2001) and Kauffmann et al. (2003) are represented by solid and short-dashed lines, respectively; finally (iv) the demarcation line segregating between Seyferts and LINES defined by Kewley et al. (2001) is shown as a long-dashed line. The color figure can be viewed online.

and (iii) late-spirals, or spirals with weak or no bulge (Sc/Sd). Finally, each row corresponds to galaxies with a different stellar mass, from high-mass ($10^{11-13.5}$M$_\odot$) to low-mass ($10^{7-9.5}$M$_\odot$). This way, any panel at a certain column and row represents the BPT diagram for galaxies with a particular morphology and stellar mass. In

addition in each panel is included the location of the azimuthal average [OIII]/Hβ and [NII]/Hα value at different galactocentic distances.

Figure 9 shows very similar patterns and distributions as those already reported by Sánchez (2020) and Sánchez et al. (2022). For the full sub-sample (top-left panel) the three studies show the highest densities along the known location of either classical H II regions (e.g. Osterbrock 1989) or SF galaxies (e.g. Kauffmann et al. 2003). The highest values of EW(Hα) (>10Å) are found at these locations too, corresponding to galactocentric distances >0.7 *Re* (i.e., to the disk of galaxies). The distribution presents an extension of much lower density towards the right-side of the diagram, where the EW(Hα) presents the lowest average values (≈1Å), corresponding to the inner regions of galaxies (<0.5 *Re*, i.e., the bulges). This pattern agrees with our current understanding of the dominant ionizing processes in galaxies (e.g. Sánchez et al. 2021). While the ionization in the disk is dominated by the contribution of OB young massive stars, tracers of recent SF processes, the inner region is dominated by a LINER-like ionization (Heckman 1987) produced most probably by Hot-Evoled Low-Mass/post-AGB stars (HOLMES; Binette et al. 1994; Flores-Fajardo et al. 2011; Singh et al. 2013; Belfiore et al. 2017a; Lacerda et al. 2018). Thus, the radial pattern of line ratios is primarily dominated by a change in the dominant ionizing source. Besides that, there is an additional change in the line ratios from the inside-out within the disk regions of galaxies, spanning from the bottom-right (for *R*≈0.6 *Re*) towards the upper-left (for *R*≈2 *Re*) regions of higher density. This additional pattern is induced by a general decline of the metal abundances from the inside-out that it observed in the average population of spiral galaxies (e.g. Sánchez et al. 2014; Sánchez 2020).

The main result from this exploration is that the dominant ionizing source is traced by the dominant stellar population. Therefore, as the star-formation history, final stellar composition, and inside-out distribution within galaxies depend on the current morphology and accumulated stellar mass (e.g. González Delgado et al. 2014; García-Benito et al. 2017; Sánchez 2020), and thus the described patterns will be strongly modulated by those two parameters. This is evident in Figure 9. Massive and early-type galaxies (E/S0 and $M_\star \approx 10^{11-13.5}$ $M_\odot$), those presenting the older and less diverse stellar population, present the lowest and more homogeneous distribution of EW(Hα), with most of the ionized regions covering a regime between the center and the right-side of the BPT diagram. We should stress that, contrary to the usual perception their ionized regions are not all restricted to the regime above the classical demarcation lines adopted to separate between SF and non-SF ionization (e.g. Kewley et al. 2001; Kauffmann et al. 2003), despite the fact that no star formation (and therefore, no young OB-stars) are present in these galaxies. As indicated before, their ionization is dominated by either HOLMES/post-AGB stars (the presence of a significant contribution of low-/mid-velocity shocks also cannot be excluded; and see Dopita et al. 1996). Early-type of lower stellar masses present a larger fraction of ionization in the H II/SF regime of the diagram, although the presence of LINER-like ionization is observed at any stellar mass. Rejuvenation induced by the capture of less massive, gas rich, galaxies or the effect of the slow dimming of a disk remant could explain this ionization (Gomes et al. 2016; Oyarzun et al. 2019).

On the other hand, low massive and late-type galaxies (Sc/Sd and $M_\star \approx 10^{7-9.5}$ $M_\odot$), those presenting the youngest stellar populations, present the highest EW(Hα) values, with a significant variation from the inside-out (from 10Å to 100Å). Their ionized regions are essentially restricted to the classical location of H II regions, well below the Kewley et al. (2001) demarcation line, and in most of the cases even below the more restrictive Kauffmann et al. (2003) one. We discussed before that their line ratios change from the inside-out following a negative galactocentric abundance gradient. Following the same trend described for eary-type galaxies (E/S0) discussed before, late-type galaxies of higher stellar mass, being still dominated by the presence of young massive stars, present a clear increase of harder ionizations, with the distribution steadily shifting towards the so-called intermediate and LINER-like region of the diagram (i.e., they present an increase in the [N II]/Hα line ratio).

Finally, early-spirals with MW-like stellar masses (Sa/Sb $M_\star \approx 10^{10.5-11}$ $M_\odot$), those with the strongest gradient in the stellar populations from the inside-out, present the highest range of EW(Hα) too (from ≈1Å to ≈100Å). Their ionized regions cover the widest range of possible line ratios, with a location similar to those of massive/early-type galaxies (for their central regions), and similar to those of less-massive/late-type galaxies (for the outer regions). This highlights again the strong connection between the dominant stellar population and the observed properties of the ionized gas (i.e., line ratios). Like in the two previous cases (E/S0 and Sc/Sb), the low mass early-type spirals present an ionization more dominated by young massive stars, while the high mass ones present a stronger component of intermediate/LINER-like ionization.

As indicated before, all these patterns are very similar to those described in Sánchez (2020) and Sánchez et al. (2022). However, there are subtle but relevant differences, most of them related to the average radial distribution (traced by the grey solid circles in Figure 9).

In the two previous explorations the radial trends were well defined for all morphological subsamples for stellar masses above $10^{10.5}M_{\odot}$. These trends are very similar to the one reported here, describing a shift from the right-side in the central regions (more to the LINER-like in the presene of a bulge or for early-type galaxies) towards the left-side in the outer ones (more prominent and following the loci of classical H II regions for disk dominated galaxies). However, below that mass in both previous studies the trends are less clear, or they directly bend or reverse from this average one observed in the current dataset. This is more evident for late-type/low-mass galaxies (bottom-right panel, Figure 9). As this radial trend, for this particular sub-sample, is determined by a decrease (increase) in the oxygen abundance (ionization strength) from the inside-out, we consider that the distributions observed when using the current dataset fit better with our current understanding of the chemical structure of disk galaxies than the previously reported ones.

We consider that most probably the source of the discrepancy is in the analyzed data themselves. In the case of Sánchez (2020) an heterogeneous compilation of IFS data from different surveys was used, including data of high spatial resolution (AMUSING++; López-Cobá et al. 2020), but also data from CALIFA v2.2, MaNGA (Bundy et al. 2015) and SAMI (Croom et al. 2012), that indeed dominate the statistics. Despite the effort in that review to homogenize the dataset and select only the well resolved data, as we show in §4.3.2, the improved spatial resolution resolution has a clear effect in the exploration of the properties of the ionized gas. The fact that the results presented in Sánchez et al. (2022), using the MaNGA data with lower spatial resolution (even lower in physical terms, due to the average redshift of that sample), present the same discrepancies, reinforces that suspicion.

5. SUMMARY AND CONCLUSIONS

Along this article we present one of the largest and better quality distributions of spatial resolved spectrocopic properties of galaxies obtained using IFS data. Comparing with the most recent distributions of similar products, like the results from the analysis using `pyPipe3D` on the final DR of the MaNGA IFS galaxy survey (Sánchez et al. 2022), we acknowledge that this latter distribution covers a much larger number of galaxies (≈10,000). However, the number of independent spectra provided by that survey (≈2 millions) is only a factor of two larger than the one provided here. This implies that, on average, eCALIFA provides with nearly five times more sampled spatial elements per galaxy. In addition, the MaNGA covers up to 1.5 *Re* for ≈2/3 of the sample, while eCALIFA covers more than 2 *Re* for ≈85% of the galaxies (Sánchez 2020, Sanchez et al. 2023). Finally, the new reduction introduced by Sanchez et al. (2023) improved the spatial resolution of the original CALIFA data from 2.4″/FWHM (≈700 pc) to ≈1.0-1.5″/FWHM (≈300 pc). In summary, despite the more limited number of galaxies, the spatial sampling and coverage of the optical extension of galaxies is significantly better, in comparison to other IFS surveys with larger galaxy samples.

We describe along this article the analysis performed on this data set, particularly emphasizing the description of the changes introduced in the analysis with respect to previous similar explorations. For each galaxy we deliver a single FITS file comprising different extensions in which each of them includes the spatial distributions of the different physical and observational quantities derived by the analysis. We present a detailed description of each of these extensions, illustrating their content using the results for the galaxy NGC 2906 as a showcase. Finally, we extract for each galaxy a set of integrated and/or characteristic parameters and, when required, the slopes of their radial gradients. We provide an additional catalog containing over 550 derived quantities for each object in the data set.

We illustrate the content of this new set of dataproducts by exploring (i) the properties of the ionized gas in the archetypal galaxy NGC 2906, and (ii) the distribution across the classical BPT diagnostic diagram of the spatial resolved ionized gas for the full sample, segregated by morphology and stellar mass. In both cases, the effects of the improved spatial resolution are appreciated, in particular the ability to detect H II regions and to recover radial trends that were less evident or not directly observed when using data of coarser resolution.

The complete set of data products and the catalog of invidual quantities is freely distributed for its use by the communitty as part of the eCALIFA data release [13].

We thank the referee for his/her suggestions that have improved the content of the current manuscript.

S.F.S. thanks the PAPIIT-DGAPA AG100622 project. J.K.B.B. and S.F.S. acknowledge support from the CONACYT grant CF19-39578. R.G.B. acknowledges financial support from the grants CEX2021-001131-S funded by MCIN/AEI/10.13039/501100011033, SEV-2017-0709, and to PID2019-109067-GB100. L.G. acknowledges financial support from the Spanish Ministerio de Ciencia e Innovación (MCIN), the Agencia Estatal de Investigación (AEI) 10.13039/501100011033, and the European Social Fund (ESF) "Investing in your future" under the 2019 Ramón y Cajal program

[13] `http://ifs.astroscu.unam.mx/CALIFA_WEB/public_html/`

TABLE 7

FLUX_ELINES_LONG EXTENSION: ANALYZED EMISSION LINES

#I	λ (Å)	Id	#I	λ (Å)	Id	#I	λ (Å)	Id	#I	λ (Å)	Id	#I	λ (Å)	Id
0	3726.03	[OII] *	26	4287.4	[FeII]	52	4754.83	[FeIII]	78	5158.0	[FeII]	104	5577.34	[OI]
1	3728.82	[OII] *	27	4340.49	Hγ*	53	4769.6	[FeIII]	79	5158.9	[FeVII]	105	5631.1	[FeVI]
2	3734.37	HI*	28	4358.1	[FeII]	54	4774.74	[FeII]	80	5176.0	[FeVI]	106	5677.0	[FeVI]
3	3750.15	HI	29	4358.37	[FeII]	55	4777.88	[FeIII]	81	5184.8	[FeII]	107	5720.7	[FeVII]
4	3758.9	[FeVII]	30	4359.34	[FeII]	56	4813.9	[FeIII]	82	5191.82	[ArIII]	108	5754.59	[NII]
5	3770.63	HI	31	4363.21	[OIII]	57	4814.55	[FeII]	83	5197.9	[NI]*	109	5876.0	HeI*
6	3797.9	HI*	32	4413.78	[FeII]	58	4861.36	Hβ*	84	5200.26	[NI]*	110	5889.95	NaI*
7	3819.61	HeI	33	4414.45	[FeII]	59	4881.11	[FeIII]	85	5220.06	[FeII]	111	5895.92	NaI*
8	3835.38	HI	34	4416.27	[FeII]	60	4889.63	[FeII]	86	5261.61	[FeII]	112	6087.0	[FeVII]
9	3868.75	[NeIII]	35	4452.11	[FeII]	61	4893.4	[FeVII]	87	5268.88	[FeII]	113	6300.3	[OI]*
10	3888.65	HeI*	36	4457.95	[FeII]	62	4905.35	[FeII]	88	5270.3	[FeIII]	114	6312.06	[SIII]
11	3889.05	HI*	37	4470.29	[FeII]	63	4921.93	HeI	89	5273.38	[FeII]	115	6363.78	[OI]
12	3933.66	CaII	38	4471.48	HeI	64	4924.5	[FeIII]	90	5277.8	[FeVI]	116	6374.51	[FeX]
13	3964.73	HeI*	39	4474.91	[FeII]	65	4930.5	[FeIII]	91	5296.84	[FeII]	117	6435.1	[ArV]
14	3967.46	[NeIII]*	40	4485.21	[NiII]	66	4942.5	[FeVII]	92	5302.86	[FeXIV]	118	6548.05	[NII]*
15	3968.47	CaII *	41	4562.48	[MgI]	67	4958.91	[OIII]*	93	5309.18	[CaV]	119	6562.85	Hα*
16	3970.07	Hϵ*	42	4571.1	MgI]	68	4972.5	[FeVI]	94	5333.65	[FeII]	120	6583.45	[NII]*
17	4026.19	HeI	43	4632.27	[FeII]	69	4973.39	[FeII]	95	5335.2	[FeVI]	121	6678.15	HeI
18	4068.6	[SII]	44	4658.1	[FeIII]	70	4985.9	[FeIII]	96	5376.47	[FeII]	122	6716.44	[SII]*
19	4076.35	[SII]	45	4685.68	HeII	71	5006.84	[OIII]*	97	5411.52	HeII	123	6730.82	[SII]*
20	4101.77	Hδ*	46	4701.62	[FeIII]	72	5015.68	HeI*	98	5412.64	[FeII]	124	6855.18	FeI
21	4120.81	HeI	47	4711.33	[ArIV]	73	5039.1	[FeII]	99	5424.2	[FeVI]	125	7005.67	[ArV]
22	4177.21	[FeII]	48	4713.14	HeI	74	5072.4	[FeII]	100	5426.6	[FeVI]	126	7065.19	HeI
23	4227.2	[FeV]	49	4724.17	[NeIV]	75	5107.95	[FeII]	101	5484.8	[FeVI]	127	7135.8	[ArIII]*
24	4243.98	[FeII]	50	4733.93	[FeIII]	76	5111.63	[FeII]	102	5517.71	[ClIII]	128	7155.14	[FeII]
25	4267.0	CII	51	4740.2	[ArIV]	77	5145.8	[FeVI]	103	5527.33	[FeII]	129	7171.98	[FeII]

#I is the running index described in Tab. 6, and Id is a label to identify the emission lines the is the label to each emission line included in the FLUX_ELINES_LONG extension. * emission lines most frequently detected in galaxies, according to Sánchez et al. (2022), for which we distribute the characteristic value (value at the effective radius) and the slope of its radial gradient (§3.4).

RYC2019-027683-I and the PID2020-115253GA-I00 HOSTFLOWS project, from Centro Superior de Investigaciones Científicas (CSIC) under the PIE project 20215AT016, and the program Unidad de Excelencia María de Maeztu CEX2020-001058-M.

This study uses data provided by the Calar Alto Legacy Integral Field Area (CALIFA) survey (http://califa.caha.es/). Based on observations collected at the Centro Astronómico Hispano Alemán (CAHA) at Calar Alto, operated jointly by the Max-Planck-Institut für Astronomie and the Instituto de Astrofísica de Andalucía (CSIC).

This research made use of Astropy,[14] a community-developed core Python package for Astronomy (Astropy Collaboration et al. 2013, 2018).

[14] http://www.astropy.org

APPENDIX

A. LIST OF EMISSION LINES USING THE MOMENT ANALYSIS

As indicated before, we perform the moment analysis described in Sec 3.1.3 over two different list of emission lines, whose results are distributed in the FLUX_ELINES and FLUX_ELINES_LONG extensions (§4.1). In the case of the FLUX_ELINES extension we use the list of emission lines distributed in Sánchez et al. (2016b), Table 1 of that article. For the FLUX_ELINES_LONG extension the list of emission lines included in Table 7 was analyzed. For each emission line we include in this table a running index I that defines the channel in which each parameter is included (as described in Tab. 6), together with its rest-frame wavelength and an Id to identify each line. The reported wavelegnths of these emission lines were extracted from Fesen & Hurford (1996).

B. LIST OF INTEGRATED AND CHARACTERISTIC PARAMETRERS

Table 8 lists the complete set of integrated, characteristic parameters and radial gradient slopes distributed for each analyzed data cube, described in §3.4 and included in the `eCALIFA.pyPipe3D.fits` FITs file[15]. For each parameter we include the column in which the information in the FITs file table is stored, the name of the parameter, its units (when required) and a brief description.

TABLE 8

INTEGRATED AND CHARACTERISTIC PARAMETERS DELIVERED FOR EACH ANALYZED DATA CUBE*

#	parameter name	units	Description
0	ID	–	None
1	cubename	–	eCALIFA name of the data cube
2	galaxy	–	eCALIFA name of the galay
3	Re_arc	arcsec	Adopted effective radius in arcsec
4	FoV	–	Ratio between the diagonal radius of the cube and Re
5	redshift	–	Redshift of the galaxy derived by `pyPipe3D`
6	DL	Mpc	Adopted luminosity distance
7	DA	Mpc	Adopted angular-diameter distance
8	PA	degrees	Adopted position angle in degrees
9	ellip	–	Adopted ellipticity
10	Re_kpc	kpc	Effective radius in kpc
11	log_Mass	$\log(M_\odot)$	Integrated stellar mass in units of the solar mass in logarithm scale
12	e_log_Mass	$\log(M_\odot)$	Error of the integrated stellar mass in logratihm-scale
13	log_SFR_Ha	–	–
14	e_log_SFR_Ha	–	–
15	log_SFR_ssp	$\log(M_\odot\ yr^{-1})$	Integrated SFR derived from the SSP analysis t<32Myr
16	e_log_SFR_ssp	–	–
17	log_NII_Ha_cen	–	Logarithm of the [NII]6583/Hα line ratio in the central aperture
18	e_log_NII_Ha_cen	–	Error in the logarithm of the [NII]6583/Hα line ratio
19	log_OIII_Hb_cen	–	Logarithm of the [OIII]5007/Hβ line ratio in the central aperture
20	e_log_OIII_Hb_cen	–	Error in the logarithm of the [OIII]5007/Hβ line ratio
21	log_SII_Ha_cen	–	Logarithm of the [SII]6717+6731/Hα line ratio in the central aperture
22	e_log_SII_Ha_cen	–	Error in the logarithm of the [SII]6717/Hα line ratio
23	log_OII_Hb_cen	–	Logarithm of the [OII]3727/Hβ line ratio in the central aperture
24	e_log_OII_Hb_cen	–	Error in the logarithm of the [OII]3727/Hβ line ratio
25	EW_Ha_cen	Å	EW of Hα in the central aperture
26	e_EW_Ha_cen	Å	Error of the EW of Hα in the central aperture
27	ZH_LW_Re_fit	dex	LW metallicity of the stellar population at Re, normalized to the solar value, in logarithm scales
28	e_ZH_LW_Re_fit	dex	Error in the luminosity weighted metallicity of the stellar population
29	alpha_ZH_LW_Re_fit	dex/Re	Slope of the gradient of the LW metallicity of the stellar population
30	e_alpha_ZH_LW_Re_fit	dex/Re	Error of the slope of the gradient of the LW log-metallicity
31	ZH_MW_Re_fit	dex	MW metallicity of the stellar population at Re, normalized to the solar value, in logarithm scales
32	e_ZH_MW_Re_fit	dex	Error in the mass weighted metallicity of the stellar population
33	alpha_ZH_MW_Re_fit	dex/Re	Slope of the gradient of the MW log-metallicity of the stellar population

*The full table can be viewed online in `https://www.astroscu.unam.mx/rmaa/RMxAA..60-1/PDF/RMxAA..60-1_ssanchez-IV-Table8.pdf`.

[15] `http://ifs.astroscu.unam.mx/CALIFA/V500/v2.3/tables/`

REFERENCES

Angthopo, J., del Moral-Castro, I., Ferreras, I., García-Lorenzo, B., & Ramos Almeida, C. 2022, MNRAS, 515, 378, https://doi.org/10.1093/mnras/stac1655

Astropy Collaboration, Price-Whelan, A. M., SipHocz, B. M., et al. 2018, AJ, 156, 123, https://doi.org/10.3847/1538-3881/aabc4f

Astropy Collaboration, Robitaille, T. P., Tollerud, E. J., et al. 2014, A&A, 558, 33, https://doi.org/10.1051/0004-6361/201322068

Baldwin, J. A., Phillips, M. M., & Terlevich, R. 1981, PASP, 93, 5, https://doi.org/10.1086/130766

Barrera-Ballesteros, J. K., Heckman, T., Sánchez, S. F., et al. 2018, ApJ, 852, 74, https://doi.org/10.3847/1538-4357/aa9b31

Barrera-Ballesteros, J. K., Sánchez, S. F., Espinosa-Ponce, C., et al. 2022, arXiv:2206.07058, https://doi.org/10.48550/arXiv.2206.07058

Barrera-Ballesteros, J. K., Sánchez, S. F., Heckman, T., et al. 2021, arXiv:2101.04683, https://doi.org/10.48550/arXiv.2101.04683

Barrera-Ballesteros, J. K., Utomo, D., Bolatto, A. D., et al. 2020, MNRAS, 492, 2651, https://doi.org/10.1093/mnras/stz3553

Belfiore, F., Maiolino, R., Maraston, C., et al. 2017a, MNRAS, 466, 2570, https://doi.org/10.1093/mnras/stw3211

Belfiore, F., Maiolino, R., Tremonti, C., et al. 2017b, MNRAS, 469, 151, https://doi.org/10.1093/mnras/stx789

Belfiore, F., Santoro, F., Groves, B., et al. 2022, A&A, 659, 26, https://doi.org/10.1051/0004-6361/202141859

Binette, L., Magris, C. G., Stasińska, G., & Bruzual, A. G. 1994, A&A, 292, 13

Bland-Hawthorn, J. 1995, PASA, 12, 190, https://doi.org/10.1017/S1323358000020269

Bluck, A. F. L., Maiolino, R., Sánchez, S., et al. 2020, MNRAS, 492, 96, https://doi.org/10.1093/mnras/stz3264

Boardman, N., Wild, V., Heckman, T., et al. 2012, MNRAS, 520, 4301, https://doi.org/10.1093/mnras/stad277

Bruzual A., G. 1983, ApJ, 273, 105, https://doi.org/10.1086/161352

Bundy, K., Bershady, M. A., Law, D. R., et al. 2015, ApJ, 798, 7, https://doi.org/10.1088/0004-637X/798/1/7

Camps-Fariña, A., Sanchez, S. F., Lacerda, E. A. D., et al. 2021, MNRAS, 504, 3478, https://doi.org/10.1093/mnras/stab1018

Camps-Fariña, A., Sánchez, S. F., Mejía-Narváez, A., et al. 2022, arXiv:2203.01159, https://doi.org/10.48550/arXiv.2203.01159

Cano-Díaz, M., Sánchez, S. F., Zibetti, S., et al. 2016, ApJ, 821, 26, https://doi.org/10.3847/2041-8205/821/2/L26

Cardelli, J. A., Clayton, G. C., & Mathis, J. S. 1989, ApJ, 345, 245, https://doi.org/10.1086/167900

Chambers, K. C., Magnier, E. A., Metcalfe, N., et al. 2016, arXiv:1612.05560, https://doi.org/10.48550/arXiv.1612.05560

Cid Fernandes, R., Carvalho, M. S., Sánchez, S. F., de Amorim, A., & Ruschel-Dutra, D. 2021, MNRAS, 502, 1386, https://doi.org/10.1093/mnras/stab059

Cid Fernandes, R., Pérez, E., García Benito, R., et al. 2013, A&A, 557, 86, https://doi.org/10.1051/0004-6361/201220616

Cid Fernandes, R., Stasińska, G., Mateus, A., & Vale Asari, N. 2011, MNRAS, 413, 1687, https://doi.org/10.1111/j.1365-2966.2011.18244.x

Courteau, S., de Jong, R. S., & Broeils, A. H. 1996, ApJ, 457, 73, https://doi.org/10.1086/309906

Croom, S. M., Lawrence, J. S., Bland-Hawthorn, J., et al. https://doi.org/10.1111/j.1365-2966.2011.20365.x

D'Agostino, J. J., Kewley, L. J., Groves, B. A., et al. 2019, MNRAS, 487, 4153, https://doi.org/10.1093/mnras/stz1611

Dopita, M. A., Koratkar, A. P., Evans, I. N., 1996, ASPC 103, The Physics of Liners in view of recent observations, ed. M. Eracleous, A. Koratkar, and L. Ho, 44

Emsellem, E., Cappellari, M., Krajnović, D., et al. 2011, MNRAS, 414, 888, https://doi.org/10.1111/j.1365-2966.2011.18496.x

Emsellem, E., Cappellari, M., Krajnović, D., et al. 2007, MNRAS, 379, 401, https://doi.org/10.1111/j.1365-2966.2007.11752.x

Emsellem, E., Schinnerer, E., Santoro, F., et al. 2022, A&A, 659, 191, https://doi.org/10.1051/0004-6361/202141727

Espinosa-Ponce, C., Sánchez, S. F., Morisset, C., et al. 2020, MNRAS, 494, 1622, https://doi.org/10.1093/mnras/staa782

Fesen, R. A. & Hurford, A. P. 1996, ApJS, 106, 563, https://doi.org/10.1086/192348

Flewelling, H. A., Magnier, E. A., Chambers, K. C., https://doi.org/10.3847/1538-4365/abb82d

Flores-Fajardo, N., Morisset, C., Stasińska, G., & Binette, L. 2011, MNRAS, 415, 2182, https://doi.org/10.1111/j.1365-2966.2011.18848.x

Gaia Collaboration, Brown, A. G. A., Vallenari, A., et al. 2021, A&A, 649, 1, https://doi.org/10.1051/0004-6361/202039657

Gaia Collaboration, Prusti, T., de Bruijne, J. H. J., et al. 2016, A&A, 595, 1, https://doi.org/10.1051/0004-6361/201629272

Galbany, L., Anderson, J. P., Sánchez, S. F., et al. 2018, ApJ, 855, 107, https://doi.org/10.3847/1538-4357/aaaf20

García-Benito, R., González Delgado, R. M., Pérez, E., et al. 2017, A&A, 608, 27, https://doi.org/10.1051/0004-6361/201731357

García-Benito, R., Zibetti, S., Sánchez, S. F., et al. 2015, A&A, 576, 135, https://doi.org/10.1051/0004-6361/201425080

Gomes, J. M., Papaderos, P., Vílchez, J. M., et al. 2016, A&A, 585, 92, https://doi.org/10.1051/0004-6361/201525974

González Delgado, R. M., Pérez, E., Cid Fernandes, R., et

al. 2014, A&A, 562, 47, https://doi.org/10.1051/0004-6361/201322011
González Delgado, R. M., Pérez, E., Cid Fernandes, R., et al. 2017, A&A, 607, 128, https://doi.org/10.1051/0004-6361/201730883
Gorgas, J., Cardiel, N., Pedraz, S., & González, J. J. 1999, A&AS, 139, 29, https://doi.org/10.1051/aas:1999375
Guidi, G., Casado, J., Ascasibar, Y., et al. 2018, MNRAS, 479, 917, https://doi.org/10.1093/mnras/sty1480
Heckman, T. M. 1987, IAUS 121, Observational Evidence of Activity in Galaxies, ed. E.E. Khachikian, K. J. Fricke and J. Melnick (Kluwer Academic Publishers, Dordrecht) 421
Heckman, T. M., Armus, L., & Miley, G. K. 1990, ApJS, 74, 833, https://doi.org/10.1086/191522
Husemann, B., Jahnke, K., Sánchez, S. F., et al. 2013, A&A, 549, 87, https://doi.org/10.1051/0004-6361/201220582
Ibarra-Medel, H. J., Avila-Reese, V., Sánchez, S. F., González-Samaniego, A., & Rodríguez-Puebla, A. 2019, MNRAS, 483, 4525, https://doi.org/10.1093/mnras/sty3256
Ibarra-Medel, H. J., Sánchez, S. F., Avila-Reese, V., et al. 2016, MNRAS, 463, 2799, https://doi.org/10.1093/mnras/stw2126
Kauffmann, G., Heckman, T. M., Tremonti, C., et al. 2003, MNRAS, 346, 1055, https://doi.org/10.1111/j.1365-2966.2003.07154.x
Kelz, A., Verheijen, M. A. W., Roth, M. M., et al. 2006, PASP, 118, 129, https://doi.org/10.1086/497455
Kennicutt, Jr., R. C. 1998, ARA&A, 36, 189, https://doi.org/10.1146/annurev.astro.36.1.189
Kewley, L. J., Dopita, M. A., Sutherland, R. S., Heisler, C. A., & Trevena, J. 2001, ApJ, 556, 121, https://doi.org/10.1086/321545
Lacerda, E. A. D., Cid Fernandes, R., Couto, G. S., et al. 2018, MNRAS, 474, 3727, https://doi.org/10.1093/mnras/stx3022
Lacerda, E. A. D., Sánchez, S. F., Cid Fernandes, R., et al. 2020 MNRAS, 492, 3073, https://doi.org/10.1093/mnras/staa008
Lacerda, E. A. D., Sánchez, S. F., Mejía-Narváez, A., et al. 2022, arXiv:2202.08027, https://doi.org/10.48550/arXiv.2202.08027
Law, D. R., Belfiore, F., Bershady, M. A., et al. 2022, arXiv:2112.11281, https://doi.org/10.48550/arXiv.2112.11281
Levy, R. C., Bolatto, A. D., Teuben, P., et al. 2018, ApJ, 860, 92, https://doi.org/10.3847/1538-4357/aac2e5
López-Cobá, C., Sánchez, S. F., Anderson, J. P., et al. 2020, AJ, 159, 167, https://doi.org/10.3847/1538-3881/ab7848
López-Cobá, C., Sánchez, S. F., Moiseev, A. V., et al. 2017, MNRAS, 467, 4951, https://doi.org/10.1093/mnras/stw3355
López Fernández, R., González Delgado, R. M., Pérez, E., et al. 2018, A&A, 615, 27, https://doi.org/10.1051/0004-6361/201732358
Lugo-Aranda, A. Z., Sánchez, S. F., Espinosa-Ponce, C., et al. RASTI, 1, 3, https://doi.org/10.1093/rasti/rzac001
Marino, R. A., Rosales-Ortega, F. F., Sánchez, S. F., et al. 2013, A&A, 559, 114, https://doi.org/10.1051/0004-6361/201321956
McCall, M. L., Rybski, P. M., & Shields, G. A. 1985, ApJS, 57, 1, https://doi.org/10.1086/190994
Osterbrock, D. E. 1989, Astrophysics of gaseous nebulae and active galactic nuclei (University Science Books)
Oyarzun, G. A., Bundy, K., Westfall, K. B., et al. 2019, ApJ, 880, 111, https://doi.org/10.48550/arXiv.1906.05298
Panter, B., Jimenez, R., Heavens, A. F., & Charlot, S. 2007, MNRAS, 378, 1550, https://doi.org/10.1111/j.1365-2966.2007.11909.x
Pérez, E., Cid Fernandes, R., González Delgado, R. M., https://doi.org/10.1088/2041-8205/764/1/L1
Pettini, M. & Pagel, B. E. J. 2004, MNRAS, 348, 59, https://doi.org/10.1111/j.1365-2966.2004.07591.x
Relaño, M., Kennicutt, Jr., R. C., Eldridge, J. J., Lee, J. C., & Verley, S. 2012, MNRAS, 423, 2933, https://doi.org/10.1111/j.1365-2966.2012.21107
Roth, M. M., Kelz, A., Fechner, T., et al. 2005, PASP, 117, 620, https://doi.org/10.1086/429877
Salpeter, E. E. 1955, ApJ, 121, 161, https://doi.org/10.1086/145971
Sánchez, S. F. 2006, AN, 327, 850, https://doi.org/10.1002/asna.200610643
_____. 2020, ARA&A, 58, 99, https://doi.org/10.1146/annurev-astro-012120-013326
Sánchez, S. F., Avila-Reese, V., Hernandez-Toledo, H., et al. 2018, RMxAA, 54, 217
Sánchez, S. F., Avila-Reese, V., Rodríguez-Puebla, A., et al. 2019, MNRAS, 482, 1557, https://doi.org/10.1093/mnras/sty2730
Sánchez, S. F., Barrera-Ballesteros, J. K., Lacerda, E., et al. 2022, ApJS, 262, 36, https://doi.org/10.3847/1538-4365/ac7b8f
Sánchez, S. F., Barrera-Ballesteros, J. K., López-Cobá, C., et al. 2019b, MNRAS, 484, 3042, https://doi.org/10.1093/mnras/stz019
Sanchez, S. F., Galbany, L., Walcher, C. J., Garcia-Benito, R., & Barrera-Ballesteros, J. K. 2023, arXiv:2304.13022, https://doi.org/10.48550/arXiv.2304.13022
Sánchez, S. F., García-Benito, R., Zibetti, S., et al. 2016a, A&A, 594, 36, https://doi.org/10.1051/0004-6361/201628661
Sánchez, S. F., Kennicutt, R. C., Gil de Paz, A., et al. 2012, A&A, 538, 8, https://doi.org/10.1051/0004-6361/201117353
Sánchez, S. F., Pérez, E., Sánchez-Blázquez, P., et al. 2016b, RMxAA, 52, 171
Sánchez, S. F., Pérez, E., Sánchez-Blázquez, P., et al. 2016c, RMxAA, 52, 21
Sánchez, S. F., Rosales-Ortega, F. F., Iglesias-Páramo, J., et al. 2014, A&A, 563, 49, https://doi.org/10.1051/0004-6361/201322343

Sánchez, S. F., Walcher, C. J., Lopez-Cobá, C., et al. 2021, RMxAA, 57, 3, https://doi.org/10.22201/ia.01851101p.2021.57.01.01

Sánchez-Menguiano, L., Sánchez, S. F., Pérez, I., et al. 2016, A&A, 587, 70, https://doi.org/10.1051/0004-6361/201527450

Sánchez-Menguiano, L., Sánchez, S. F., Pérez, I., Ruiz-Lara, T., Galbany, L., Anderson, J. P., Krühler, T., Kuncarayakti, H., & Lyman, J. D. 2018, A&A, 609, A119

Sánchez-Menguiano, L., Sánchez Almeida, J., Muñoz-Tuñón, C., et al. 2019, ApJ, 882, 9, https://doi.org/10.3847/1538-4357/ab3044

Sarmiento, R., Huertas-Company, M., Knapen, J. H., et al. 2023, arXiv:2211.11790, https://doi.org/10.48550/arXiv:2211.11790

Singh, R., van de Ven, G., Jahnke, K., et al. 2013, A&A, 558, 43, https://doi.org/10.1051/0004-6361/201322062

Vale Asari, N., Stasińska, G., Cid Fernandes, R., et al. 2009, MNRAS, 396, 71, https://doi.org/10.1111/j.1745-3933.2009.00664.x

Veilleux, S., Shopbell, P. L., & Miller, S. T. 2001, AJ, 121, 198, https://doi.org/10.1086/318046

Walcher, C. J., Wisotzki, L., Bekeraité, S., et al. 2014, A&A, 569, 1, https://doi.org/10.1051/0004-6361/201424198

Weilbacher, P. M., Monreal-Ibero, A., Verhamme, A., et al. 2018, A&A, 611, 95, https://doi.org/10.1051/0004-6361/201731669

Westfall, K. B., Cappellari, M., Bershady, M. A., et al. 2019, AJ, 158, 231, https://doi.org/10.3847/1538-3881/ab44a2

York, D. G., Adelman, J., Anderson, Jr., J. E., et al. 2000, AJ, 120, 1579, https://doi.org/10.1086/301513

J. K. Barrera-Ballesteros, E. Lacerda, and S. F. Sánchez: Instituto de Astronomía, Universidad Nacional Autonóma de México, A.P. 70-264, 04510 CDMX, México (sfsanchez@astro.unam.mx).

A. Camps-Fariña: Departamento de FíÂsica de la Tierra y Astrofísica, Universidad Complutense de Madrid, Pl. Ciencias, 1, Madrid, 28040, Madrid.

L. Galbany: Institute of Space Sciences (ICE, CSIC), Campus UAB, Carrer de Can Magrans, s/n, E-08193 Barcelona, Spain.

L. Galbany: Institut d'Estudis Espacials de Catalunya (IEEC), E-08034 Barcelona, Spain.

R. García-Benito: Instituto de Astrofísica de Andalucía (IAA/CSIC), Glorieta de la Astronomía s/n Aptdo. 3004, E-18080 Granada, Spain.